RESEARCH ARTICLE

Frequency Robust Control Application in Islanded Microgrids Considering Parametric Uncertainties and Distinct Photovoltaic Penetration Rate Scenarios

QUANG LINH LAM [1], **DELPHINE RIU**[2],
AND ANTONETA IULIANA BRATCU[3], **(Senior Member, IEEE)**

[1]Duy Tan University, Danang 550000, Vietnam
[2]CNRS, Grenoble INP (Institute of Engineering Université Grenoble Alpes), G2Elab, Université Grenoble Alpes, 38000 Grenoble, France
[3]CNRS, Grenoble INP (Institute of Engineering Université Grenoble Alpes), GIPSA-Lab, Université Grenoble Alpes, 38000 Grenoble, France

Corresponding author: Quang Linh Lam (lamquanglinh88@gmail.com)

ABSTRACT In this paper, a cascaded two-level hybrid control scheme based on multi-variable robust $\mathcal{H}_\infty$ and proportional integral control is proposed for primary frequency control of an island mode microgrid consisting of a diesel engine generator, a photovoltaic energy source, an energy storage system, and an aggregated static load. Topological and nonlinear averaged models of each subsystem are introduced, followed by linearized frequency-control-oriented modelling of the entire system. Then, for currents control, conventional proportional-integral-based tracking controllers placed on a lower control level are designed, with their reference values generated from the output of an $\mathcal{H}_\infty$-control-based upper level. A comprehensive methodology that casts the specific engineering demands of microgrid operation into the $\mathcal{H}_\infty$ control formalism is outlined. Additionally, it is demonstrated how closed-loop dynamic performance requirements must at their turn be taken into account in the initial microgrid setup and sizing, namely in appropriately choosing and rating the energy storage system. Numerical simulations performed with MATLAB®/Simulink® show the validity and effectiveness of the proposed frequency robust control technique in the presence of multiple photovoltaic power step changes on a kVA-rated microgrid. A robust performance analysis of the previously designed $\mathcal{H}_\infty$ controller is performed under numerous uncertainty levels in the steady-state value of the supercapacitor state of charge and multiple photovoltaic power step changes to determine if the closed-loop system remains robust from a performance standpoint around its nominal design. The $\mathcal{H}_\infty$ control design procedure allows a further investigation on how to link time-domain dynamic performance specifications (e.g., desired control objectives) and frequency-domain specifications (e.g., *via* so-called weighting functions) in a systematic and optimal manner (i.e., automation for their design or expert modelling), from which an useful guide can be created for practical control engineers in the future. Distinct photovoltaic penetration rate scenarios together with respective computed $\mathcal{H}_\infty$ controllers, on the other hand, are examined to determine whether or not an $\mathcal{H}_\infty$ optimal control solution that is robust in performance to a variety of photovoltaic power step variations relative to the rated operating point can always be generated.

INDEX TERMS Energy management, multi-variable robust control, frequency ancillary service, islanded microgrids, smart electrical networks, electricity – distribution, averaged modelling, parametric uncertainties, robust performance analysis, renewable energy.

The associate editor coordinating the review of this manuscript and approving it for publication was Gab-Su Seo.

NOMENCLATURE

List of Acronyms

AC/DC	Alternating Current/Direct Current.
DER	Distributed Energy Resource.
DG	Distributed Generation.
ESS	Energy Storage System.
LMI	Linear Matrix Inequality.
LPV	Linear Parameter Varying.
MG	Microgrid.
PI/PID	Proportional Integral/Proportional Integral Derivative.
PCC	Point of Common Coupling.
PV	Photovoltaic.
PWM	Pulse-Width Modulation.
RES	Renewable Energy Source.
SoC	State of Charge.

List of Notations

ρ_e	Energy density of a source (J/kg or Wh/kg).
ρ_p	Power density of a source (W/kg).
D_{grid}	Connection grid damping constant (MW/Hz).
D'_{load}	Investigated load damping constant (MW/Hz).
f_p	Characteristic (own) frequency of a source (Hz).
H'	Investigated MG equivalent inertia constant (MW.s).
H_{grid}	Connection grid inertia constant (MW.s).
r_{PV}	PV penetration rate (%).
SoC_{sc}	Supercapacitor state of charge (%).
$W^*_{sc_{max}}$	Maximum storable energy of a source (J).
W^*_{sc}	Stored energy of a source (J).

I. INTRODUCTION

A. MICROGRID CONTROL

The concept of MGs first appears in the technical literature in [1] as a promising, cost-effective solution for integrating DERs into power systems, as they offer enhanced global reliability, increased energy efficiency, and multiple environmental and economic benefits. In this context, to ensure MG stability and suitable overall performance is a challenge of crucial importance, especially during islanded – otherwise said, isolated or autonomous, or again off-grid or stand-alone – mode, where low inertia, uncertainties, and intermittent nature of DERs play an even more constraining role [2]. Thus, compelling frequency and voltage deviations to stay within some maximally admissible ranges as imposed by stiff grid codes is of focal importance in stand-alone operation mode. Finding pertinent technological solutions to this problem has determined a large research effort being deployed lastly, out of which use of short- and medium-term ESSs – e.g., batteries, flywheels, or supercapacitors – has proved to open a promising way towards feasible implementations. The resulted new grid configurations have again emphasized the need for advanced control structures to deal with unexpected disturbances and model uncertainties.

B. LITERATURE REVIEW

Frequency and voltage control, as well as power sharing, are presently challenging topics in autonomous (islanded or stand-alone) MGs, thus requiring advanced control techniques, with robust control design being an illustrative example. Among powerful robust control design frameworks, the $\mathcal{H}_\infty$ approach is perfectly suited for offering the required flexibility in order to generally guarantee robustness to parameter uncertainties [3], [4], [5], [6], [7], [8], [9], [10], [11], topology changes [7], interaction dynamics [7], [12], system inertia and damping property uncertainties [9], [10], wide range of MG operating conditions [10], measurement noise [3], [10], dynamics of phase-locked loop with measurement delay [10], as well as robust rejection of disturbances originating from all types of source and/or load variation, including RES generation [9], [10], [13], [14], possibly nonlinear and/or unbalanced loads [6], [11], [12], [13], load harmonics [11]. $\mathcal{H}_\infty$ techniques may be successfully combined with some other well-known controller designs – e.g., droop characteristics improved by integrating power derivative and integral terms [3], multiple droop control [7], decentralized static output feedback technique [13], mixed-sensitivity optimization [3], [4], [5], [8], [12], [14], virtual-inertia-injection technique [9], [10], loop-shaping method [6], output feedback scheme [11], low-/fixed-order dynamic output feedback control [8] – to lead to well-performing results spanning from numerical simulation to hardware-in-the-loop validation test benches, potentially including suitable order reduction of the resulted controller such as to meet real-time implementation constraints. As regards storage and generation coordination in MGs frequency control [3], [4], [13], despite optimization of various trade-offs, analysis lacks controllers' robustness to model uncertainties. In [9], the output multiplicative perturbation technique is used to represent uncertainty, whereas in [10], the uncertainties are retrieved from the system in the form of structured uncertainties. When considering MGs voltage control in the presence of parallel-connected inverter-interfaced DG units, a translation of parameter uncertainty into a multiplicative output structure is proposed in [5], while [6], [11], and [12] do not take into account context-dependent uncertainty modelling or weight selection. In other works pertaining to related issues – such as flexible MG connection control for grid-tied PV generation systems [14], power sharing in a PV-wind MG [7], stability issues of an LCL-based DG unit connected to a weak grid [8] – unmodelled uncertainties can be employed as in [14], the plant can be described by a nominal model supposed norm-bounded uncertain with an integral quadratic constant as in [7], and some polytopic uncertainty can be represented as in [8] *via* a convex hull with two given vertices.

$\mathcal{H}_\infty$ techniques combined with feedback-feedforward and/or internal model robust feedback control have already been conducted in autonomous MGs or multi-MGs consisting of several DG units to improve voltage performance and robustness to parameter uncertainties [15], inter-

action dynamics [15], as well as robust rejection from micro-source output power fluctuations [16], linear/nonlinear and/or unbalanced loads [16], [17]. The proposed control scheme is designed using an extended model that incorporates various converter-MG interactions [15], whereas [16], [17] do not require any problem-dependent uncertainty modelling.

Another intriguing application for frequency/voltage control in isolated hybrid generation systems consisting of DG and storage units is the use of $\mathcal{H}_\infty$ control in conjunction with artificial-intelligence-based control, such as $\mathcal{H}_\infty$-based droop control or $\mathcal{H}_\infty$ loop shaping control *via* genetic algorithm and particle swarm optimization [18], harmony search and conventional droop based $\mathcal{H}_\infty$ control [19], μ-synthesis *via* structured linear fraction transformers and $\mathcal{H}_\infty$ loop shaping control *via* genetic algorithm and particle swarm optimization [20], Golver Doyle optimization algorithm [21], to enhance the required adaptability in terms of simplicity, stability, disturbance rejection, robustness, as well as quick convergence and easy implementation due to parameter variations [18], [19], [21], varying wind power input [18], [20], load change [18], [20], system loading breach [19], input voltage and current fluctuations [21]. The normalized coprime factorization technique is applied in [18] to represent all unstructured uncertainties in the system. However, only the controller sensitivity to system parameter uncertainties is investigated in this study. This unstructured uncertainty modelling is also adopted in [20]. When the system is subjected to multiplicative uncertainty, the stability of the closed-loop shown in [19] is explored using the small-gain theorem. The Golver Doyle optimization algorithm presented in [21] requires an augmented system extracted from the small-signal model of the DG MG.

To ameliorate the inherent defects of the above-mentioned control approaches in the face of large-signal disturbances, as well as to possess robustness and optimal frequency/voltage transient performance in controlling multi-DER voltage source converter-based autonomous MGs, mixed $\mathcal{H}_2/\mathcal{H}_\infty$ control is gradually in the spotlight. Robust mixed $\mathcal{H}_2/\mathcal{H}_\infty$ control integrated with sliding mode control [22], descriptor system $\mathcal{H}_\infty$ approach, decentralized robust servo-mechanism-based control, and hierarchical droop-based control [23], [24], constrained optimal control and regional pole placement [25], [26] have literally been studied to deal with large system parameter variations [22], unmodeled dynamics [25], exogenous, small and large-signal disturbances [22], [23], [24], [26], unbalanced and nonlinear loads [23], [24], [25], RESs fluctuation [26], so as to obtain desired performance and robustness and to provide the benefits of constant switching frequency, low total harmonic distortion [22], set point tracking, fault ride through capability [23], [24], reference commands of voltages tracking [25], effective interchange power control [26]. The plant nominal model is norm-bounded uncertain [22], whereas no problem-dependent uncertainty modelling or weight selection is adopted in [23], [24], [25], and [26].

It is of notorious evidence that islanded inverter-interfaced or AC/DC MGs are constantly submitted to external disturbance and measurement noise, therefore discrepancies between the mathematical models used in the design and the actual system always exist, thus emphasizing the crucial role of robustness in the design of control systems. Despite its wide recognition, the need for and the importance of robustness in the design of control systems have been especially put into light during the last two decades [27]. Consequently, μ-synthesis is employed as a powerful tool in the analysis and design with real unstructured [27], [28], [29], [30] or structured parametric uncertainties within both norm-bounded multiplicative and additive structure [31], [32], [33], [34], [35], as well as polytopic uncertainty [36], [37], represented in the uncertainty block by the performance criteria for multi-variable controller design purpose aiming at frequency/voltage control and stabilization while guaranteeing high levels of robustness and performance to parameter uncertainties [27], [28], [29], [31], [32], [33], [34], [35], load and RESs variations [29], [30], [31], [33], [36], [37], output disturbances and sensor noises/errors [29], [31], [34], [35], and across the whole domain of operating point variation [28], [29], MG topology change [27], [36], [37], dynamic interaction between source and load [30], all by achieving less conservativeness in the design, namely in the sense of reducing the number of constraints and trade-offs in the control system.

C. RESEARCH GAP, MOTIVATION, AND PAPER CONTRIBUTION

Systematic analysis of the above-mentioned works reveals that various mathematical modelling techniques have been exploited for robust control of frequency, power sharing and stabilization in different MG and small power system scenarios. Nonetheless, dynamic modelling for frequency robust control has not yet been thoroughly approached in the earlier investigations. Justified by this constraint, this paper provides a novel overall frequency-control-oriented model of an MG consisting of a diesel-PV-storage/converter system in the form of a nonlinear and linear state-space per-unitized expression. This further allows the formalization, design, and implementation of a comprehensive robust control system having effective and robust rejection properties under a broad range of parametric and neglected dynamics uncertainties.

The second goal of this paper is to discuss frequency stability and control challenges for stand-alone MGs that generate a significant portion of their energy from decentralized, renewable, and intermittent sources. It is shown that if suitable dynamical coordination of storages with other generation sources is achieved and saturations are avoided, then relatively small storages can significantly reduce both frequency [31] and voltage [16] variations.

Indeed, choice of a robust control design framework appears in this context as particularly suitable, because most of the parameters are submitted to *a priori* unknown variations, but within bounded intervals. Also, robustness issues

must be taken into account in order to guarantee rejection of large-magnitude fast-varying disturbances, such as load power variations, which cannot be ensured by simply employing classical PI/PID-based control. A third argument pleading for use of a robust control approach is the possibility of suitably including a multi-objective optimization into the formal control problem statement. Given the above arguments, a robust control structure, in spite of being obviously more complex, is reasonably expected to outperform conventional linear controllers, such as PI/PID, due to its flexibility ensured by more degrees of freedom.

The principal contributions of this paper to the current related research field are built upon our results in [38], [39], [40], and [41] – obtained for the considered MG's frequency robust control – in the sense that the modelling approach and the initial $\mathcal{H}_\infty$-based closed-loop robustness performance analysis have now been extended to account for distinct PV penetration rate scenarios, namely by the following points

- This paper's novelty first concerns the centralized multivariable $\mathcal{H}_\infty$-based two-layered robust control design formalism, which is proposed as solution to frequency regulation problem in the stand-alone operation mode of a diesel-PV-supercapacitor hybrid power generation system, in a coherent systematic approach based on a suitable nonlinearized or linearized control-oriented modelling and rigourous formal translation of various engineering specifications, among which the (micro) grid codes;

  The $\mathcal{H}_\infty$ controller acts as an upper control level and serves as a reference point for current controllers positioned on a lower control level. In addition, it is demonstrated how closed-loop operation requirements must be factored into the initial MG configuration and design, namely in effectively selecting and rating the ESS. In the presence of multiple PV power step changes on a kVA-rated MG, numerical simulations performed with MATLAB[®]/Simulink[®] demonstrate the validity and effectiveness of the proposed frequency robust control technique;

  Also, in this work, the designed PI and $\mathcal{H}_\infty$ controllers are implemented *via* numerical simulations under extended scenarios, to be as relevant as possible for validation purpose. Thus, in order to more precisely evaluate the domain in which the applied robust control ensures stable and robust performance, both small load step disturbances and more stressed conditions – large load step disturbances – are taken into account;

  Results briefed in this section remain thus focused on how to ensure a judicious management of storage units, in order to enhance the mixture of classical and renewable sources;

- Second, a robust performance study of the previously designed $\mathcal{H}_\infty$ controller is conducted under multiple uncertainty levels in the steady-state value of the supercapacitor state of charge and numerous PV power step

changes to iteratively enhance the design of the MG, thereby increasing the dynamic performances of the closed-loop system around its nominal design;

  The use of "fast" storages – like supercapacitors in our case – is proven as beneficial and robustly well-performing in both improving closed-loop dynamic behaviour – in primary regulation of frequency – and also in protecting other "slower" generation sources – like diesel generators or batteries – from being over-sollicited outside their "specialization" operation range, with significant gains of service time extension, as the supercapacitor state of charge can vary from empty to full without resulting in closed-loop stability or performance degradation;

- Third, distinct PV penetration rate scenarios are accounted for, wherein respective $\mathcal{H}_\infty$ controllers are computed and their robust performances are evaluated to determine whether an $\mathcal{H}_\infty$ optimal control solution subject to a variety of PV power step variations relative to the rated operating point can always be generated or not.

The remainder of this paper is structured as follows. Section II discusses MG description and choice of energy storage technology. Section III is devoted to the proposed control methodology. Dynamic performance specifications are presented in Section IV. Section V provides system modelling for $\mathcal{H}_\infty$ control. The detailed method for designing the $\mathcal{H}_\infty$ controller to ensure that the preceding dynamic performance specifications are met is described in Section VI. Section VII demonstrates a robust performance investigation of the computed $\mathcal{H}_\infty$ controller *via* a series of MATLAB[®]/Simulink[®] closed-loop time-domain simulations relative to the rated operating point or considering uncertainty levels in either the steady-state value of the supercapacitor state of charge or the PV penetration rate, and subject to a number of PV power step change scenarios. Some concluding remarks and perspectives are drawn in Section VIII.

II. MICROGRID DESCRIPTION AND CHOICE OF ENERGY STORAGE TECHNOLOGY
A. MICROGRID DESCRIPTION

Power sources within the considered MG – a diesel generator as a classical source, a PV unit as a renewable source, and an energy storage unit – are connected in parallel to a PCC and supply an aggregated static load, as shown in Fig. 1(a). Three-phase step-up transformers are used to connect the power sources, permitting unidirectional and bidirectional power flows for the PV unit and the ESS, respectively, while a three-phase step-down transformer is utilized to connect the load to the PCC. Subsection II-B will elaborate on the choice of a supercapacitor storage device for primary frequency control participation.

To facilitate frequency stability analysis, a simplified MG configuration derived from the studied MG structure is employed, as shown in Fig. 1(b). Its equivalent inertia
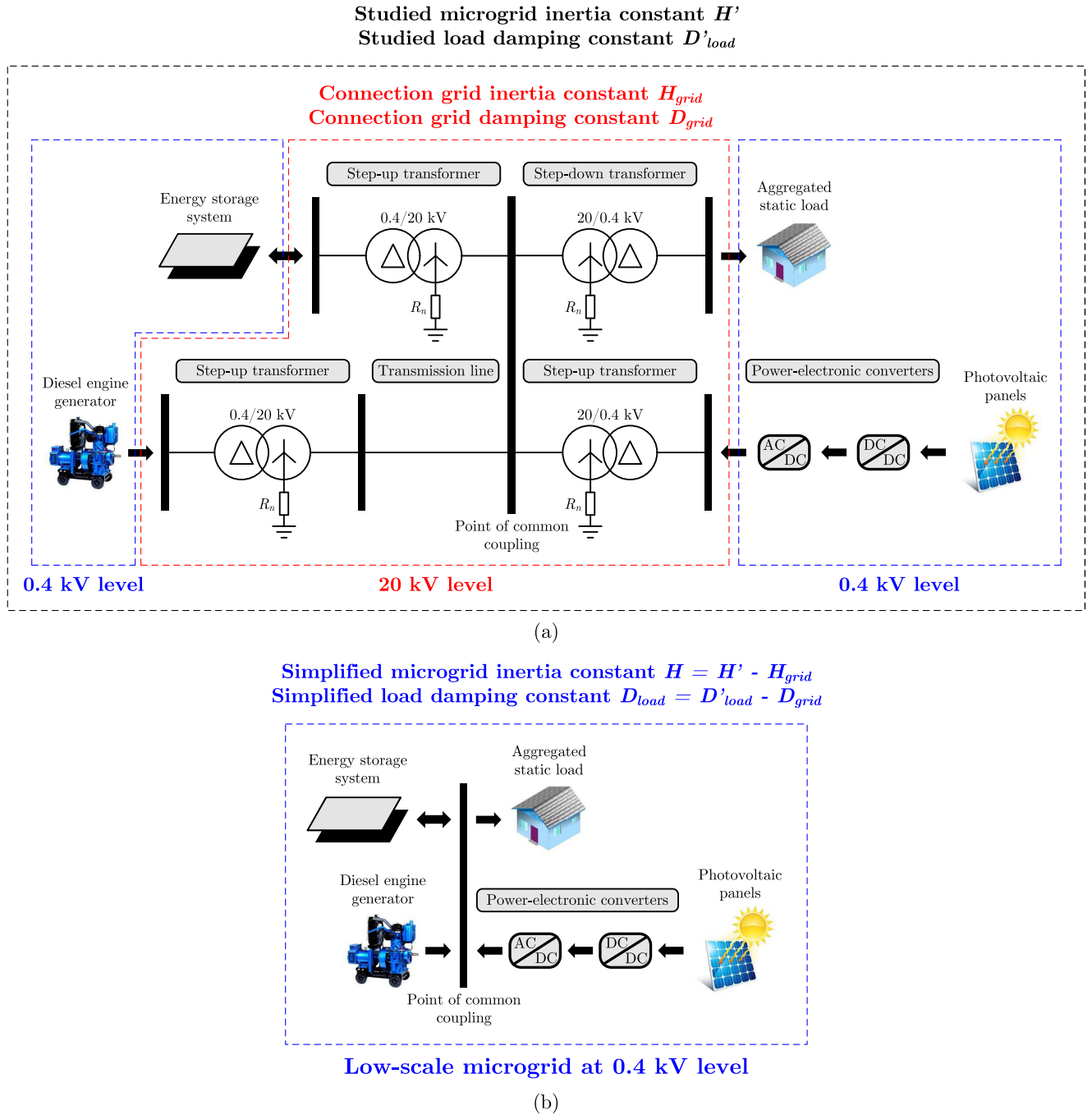
Studied microgrid inertia constant *H'*
Studied load damping constant *D'*$_{load}$

Connection grid inertia constant *H*$_{grid}$
Connection grid damping constant *D*$_{grid}$

(a)

Simplified microgrid inertia constant *H = H' - H*$_{grid}$
Simplified load damping constant *D*$_{load}$ = *D'*$_{load}$ - *D*$_{grid}$

Low-scale microgrid at 0.4 kV level

(b)

FIGURE 1. (a) Schematic diagram of the studied MG. (b) Simplified MG configuration for frequency stability analysis [40].

constant H and load damping constant D_{load} can thus be expressed as follows

$$H = H' - H_{grid}, \qquad (1)$$

$$D_{load} = D'_{load} - D_{grid}, \qquad (2)$$

where H' and H_{grid} denote the investigated MG equivalent inertia constant and connection grid inertia constant, respectively, D'_{load} and D_{grid} denote the investigated load damping constant and connection grid damping constant, respectively.

It should be noted that the frequency stability analysis will be carried out at the lower voltage level.

The diesel-PV-supercapacitor hybrid power generation system in Fig. 1(b) can be regarded as being representative enough for an autonomous MG, like the one in [42].

B. CHOICE OF ENERGY STORAGE TECHNOLOGY
Dynamic specialization of sources is best represented by Ragone's plot [43], whose a quite complete version is

resumed here in Fig. 2, where dynamic specialization range of each storage source can be identified through the relation between its energy density (specific energy) and its power density (specific power) [44]. A large span of storage technologies is illustrated

- from high-specific-energy storage sources, such as fuel cells – able to provide energy in a long term, otherwise called "energy sources" for this reason, so specialized in the low-frequency range when talking about energy variations –
- to the high-specific-power sources, such as ultracapacitors (supercapacitors) – able to provide energy very quickly, otherwise called "power sources", so specialized in the high-frequency range,

with different electrochemical storage (e.g., batteries) or mechanical storage (e.g., flywheels) technologies being placed in between.

The type of energy storage technology chosen is determined on the required services. Notion of characteristic (own) frequency f_p (Hz) of a source was introduced to quantify more precisely its dynamic specialization range

$$f_p = \frac{\rho_p}{\rho_e}, \qquad (3)$$

where ρ_p is the power density, measured in W/kg and read on the abscissa of Ragone's plot, and ρ_e is the energy density, measured in J/kg or Wh/kg and represented on the ordinate. Fig. 3 presents characteristic frequency values for some of the main storage technologies. It corresponds ideally to the solicitation frequency of a given storage technology.

It is thus clear that a given source behaves best when exploited in its specialization range – i.e., when variation spectrum of the power demand is placed around its characteristic frequency – because its reliability and lifetime are best ensured this way. Reliability requirements may impose the decision to suitably complement – otherwise said, to hybridize – a high-energy-density source, also identified as main source, by a high-power-density one, identified as auxiliary source, in order to protect the first from possible damages due to unappropriate exploitation outside its specialization range.

In any power system, the active power generation must constantly match the demand. Disturbances in this balance are compensated for by the kinetic energy of the rotating generators and motors connected to the grid, and by the self-regulating effect of the load, resulting in a variation in the system frequency f_{grid} from its setpoint value f_{grid_e}. Under small-signal conditions, the time derivative of the system frequency deviation $\Delta f_{grid} = f_{grid} - f_{grid_e}$ can be deduced from the output active power variation of sources and load [40], [45]. The storage devices used for primary frequency control are chosen based on an analysis of the transfer function between the MG frequency deviation $\Delta f_{grid}(s)$ and the active power variation $\Delta P_{diff}(s) = \underline{\Delta P_{PV}(s)} - \underline{\Delta P_{load}}(s)$ in the frequency domain. The most critical situation for frequency variation – the largest frequency deviation caused
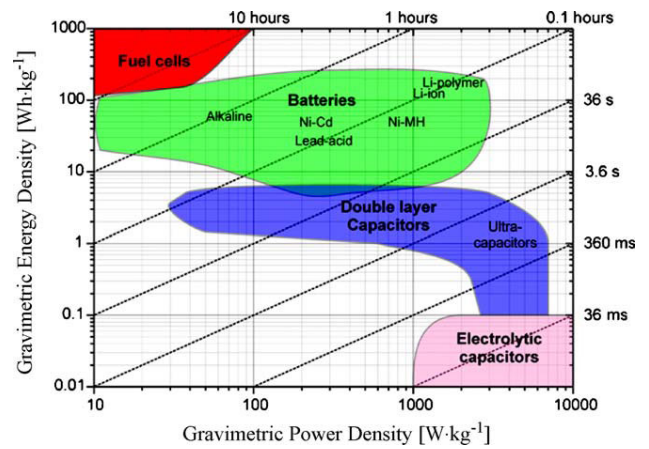

FIGURE 2. Ragone's plot: dynamic specialization of different source/storage technologies [43].
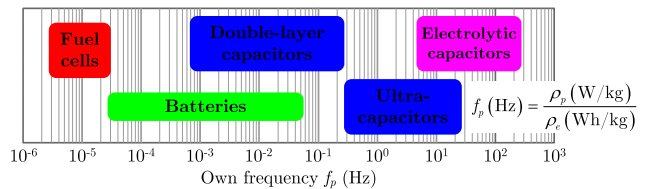

FIGURE 3. Characterization of main storage technologies by their characteristic frequencies [40].

by an active power variation – is first investigated, then an appropriate interval around the critical frequency for storage device involvement is defined. Without the storage device (i.e., $\underline{\Delta P_s}(s) = 0$), this transfer function is given by [40] and [46] (4), as shown at the bottom of the next page, where the underline indicates per-unitized values. $\underline{K_p} = 1/\underline{s_{diesel}}$ signifies the primary control with $\underline{s_{diesel}}$ denoting the droop value, $\underline{K_i}$ denotes the inverse of the response time of the secondary control, and T_{diesel} denotes the time constant of the diesel generator. $\underline{H}$ is the MG equivalent inertia constant and $\underline{D_{load}}$ is the load damping constant. If the secondary control of the diesel engine generator is disregarded (i.e., $\underline{K_i} = 0$), the transfer function in (4) takes the form [40], [46] (5), as shown at the bottom of the next page.

The Bode diagrams of the transfer functions in (4) and (5) are displayed in Fig. 4. The system with only primary control can be assumed as a low-pass filter. High-frequency power fluctuations are then filtered by the MG equivalent inertia. The DC gain of the transfer function is constant and equal to the droop value $\underline{s_{diesel}}$. Low-frequency power variations are damped by secondary control [40], [46].

1) CRITICAL FREQUENCY
A specific frequency, namely the critical (or resonant) frequency f_{cr}, around which power fluctuations $\Delta P_{diff}(s)$ can result in extremely large frequency variations $\overline{\Delta f_{grid}}(s)$, can be determined here from the modulus of the poles of the system in (4) or (5). As a result of its lower order, the system
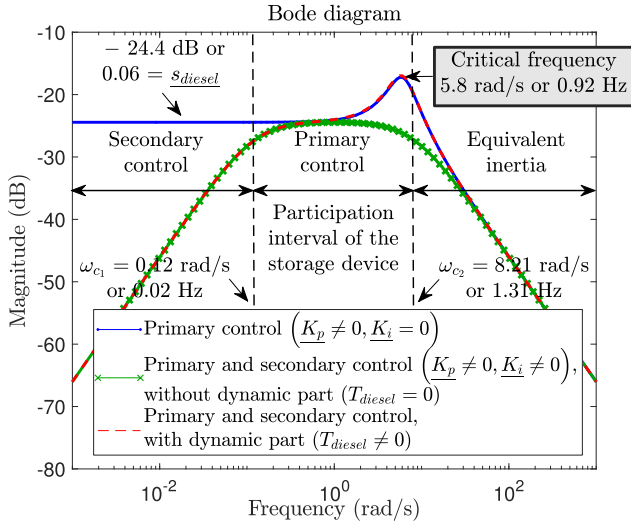
FIGURE 4. Bode diagram of the system in (4) with only primary control ($K_P \neq 0$, $K_i = 0$), both primary and secondary control ($K_P \neq 0$, $K_i \neq 0$) without the dynamic part of the diesel generator ($T_{diesel} = 0$), both primary and secondary control with the dynamic part ($T_{diesel} \neq 0$) [40].

with only primary control in (5) is utilized to establish the critical frequency [40], [46]. This system corresponds to a second-order one with a zero $z_1 = -1/T_{diesel}$, a corner frequency $\omega_n = \sqrt{\left(D_{load}s_{diesel} + 1\right) / \left(2\underline{H}T_{diesel}s_{diesel}\right)}$, and a damping ratio

$$\zeta = \frac{\left(2\underline{H} + T_{diesel}D_{load}\right)s_{diesel}}{2\sqrt{\left(D_{load}s_{diesel} + 1\right)2\underline{H}T_{diesel}s_{diesel}}}.$$

By numerical application of the MG parameter values listed in Appendix A, $\omega_n = 6.15$ rad/s and $\zeta = 0.37$ are obtained. Since $0 < \zeta < 1/\sqrt{2}$, the critical frequency may be computed as $\omega_{cr} = \omega_n\sqrt{1 - 2\zeta^2}$. By numerical application, $\omega_{cr} = 5.25$ rad/s or $f_{cr} = 0.84$ Hz are obtained. These values are approximately equal to those estimated in Fig. 4.

It is crucial to determine the critical frequency value based on whether or not the storage device is considered to be involved in secondary control. Indeed, if the storage device is utilized exclusively for primary control participation, an appropriate interval around this critical frequency value must be calculated in order to constrain the storage device bandwidth. When both primary and secondary control

of the storage device are considered concurrently, a larger bandwidth is required for its involvement, and thus the concept of this critical frequency value becomes obsolete.

As analyzed from the Bode diagrams in Fig. 4, utilizing a storage device in a medium-frequency interval around the specified critical frequency is thus appropriate for limiting MG frequency changes.

2) ADOPTED STORAGE TECHNOLOGY
Definition of cut-off frequencies for separating the frequency intervals within a storage device participation bandwidth is useful, as it is further utilized to select an appropriate storage technology. To compute these cut-off frequencies, the diesel generator dynamics are first neglected (i.e., $T_{diesel} = 0$) in order to simplify the transfer function in (4) as follows [40], [46]

$$\frac{\Delta f_{grid}(s)}{\Delta P_{diff}(s)} = \frac{s/K_i}{\frac{2\underline{H}}{K_i}s^2 + \frac{D_{load} + K_p}{K_i}s + 1}, \quad (6)$$

which corresponds to a second-order system with a zero at the origin, a corner frequency $\omega_n = \sqrt{K_i/2\underline{H}}$, and a damping ratio $\zeta = \left(D_{load} + K_p\right) / \left(2\sqrt{2\underline{H}K_i}\right)$. The magnitude of this transfer function is illustrated in Fig. 4. Given that ζ equals 4.17 and $A_F = \left(D_{load} + K_p\right)^2 - 8\underline{H}K_i = 261.78 > 0$ for the considered MG, two cut-off frequencies denoted by $\omega_{c_{1,2}}$ may be computed as follows [40], [46]

$$\omega_{c_{1,2}} = \frac{1}{4\underline{H}}\left| -\left(D_{load} + K_p\right) \right.$$
$$\left. \pm \sqrt{\left(D_{load} + K_p\right)^2 - 8\underline{H}K_i} \right|. \quad (7)$$

By substituting MG parameter values into (7), the low cut-off frequency $\omega_{c_1} = 0.12$ rad/s (or $f_{c_1} = 0.02$ Hz) and the high cut-off frequency $\omega_{c_2} = 8.21$ rad/s (or $f_{c_2} = 1.31$ Hz) are obtained. As analyzed in Fig. 4, the dynamic part mostly impacts the medium-frequency zone associated with primary control and has a negligible effect on the cut-off frequencies [40], [46]. Hence, the frequency interval $f_c \in$ [0.02, 1.31] Hz is chosen for the primary control involvement of the storage device. According to Ragone's plot [43], supercapacitor storage technology with its own frequency $f_p \in$

$$\frac{\Delta f_{grid}(s)}{\Delta P_{diff}(s)} = \frac{\left(T_{diesel}s + 1\right)s}{2\underline{H}T_{diesel}s^3 + \left(2\underline{H} + T_{diesel}D_{load}\right)s^2 + \left(D_{load} + K_p\right)s + K_i}, \quad (4)$$

$$\frac{\Delta f_{grid}(s)}{\Delta P_{diff}(s)} = \frac{\left(T_{diesel}s + 1\right)s_{diesel}}{2\underline{H}T_{diesel}s_{diesel}s^2 + \left(2\underline{H} + T_{diesel}D_{load}\right)s_{diesel}s + D_{load}s_{diesel} + 1}$$
$$= \frac{1}{D_{load}s_{diesel} + 1}\frac{\left(T_{diesel}s + 1\right)s_{diesel}}{\frac{2\underline{H}T_{diesel}s_{diesel}}{D_{load}s_{diesel} + 1}s^2 + \frac{\left(2\underline{H} + T_{diesel}D_{load}\right)s_{diesel}}{D_{load}s_{diesel} + 1}s + 1}. \quad (5)$$
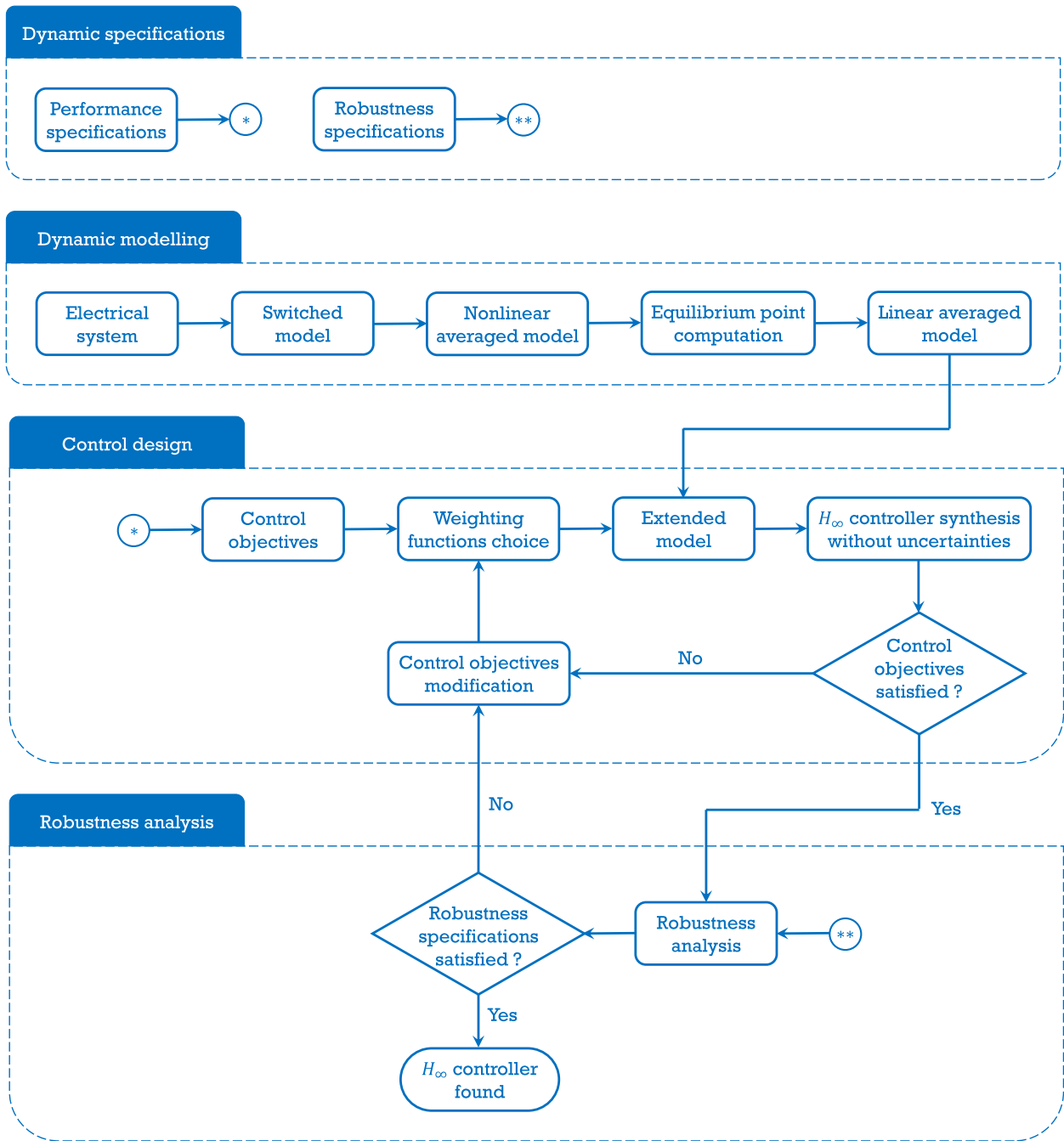
FIGURE 5. Proposed control methodology inspired from [47].

[0.00069, 27.78] Hz best matches the identified frequency interval and is thus selected for primary control involvement.

III. PROPOSED CONTROL METHODOLOGY

A generalized methodology for controller design that is based on $\mathcal{H}_\infty$ control and takes robustness into account is proposed in this work. Then, it enables time savings during the design process as the optimal controller is determined for the defined dynamic specifications (e.g., performance and robustness).

This methodology is summarized in Fig. 5 and can be divided into four steps, which are explained below [47]

- First, performance and robustness levels are specified by the designer in accordance with standards and control objectives expressed in terms of required steady-state and dynamic performance within system constraints and natural temporal response;
- Afterwards, dynamic equations and equivalent averaged models of power-electronic converters are used to

describe the behavior of the electrical system. By linearizing these equations for a given steady-state point – generally, such point characterizes the rated values of interest variables (like frequency and DC-link voltages) – a linear state-space model can be obtained. Validation of open-loop systems can be accomplished by the use of a topological model or through real-world system tests;

- To respect performance, a control architecture is then designed for the considered steady-state point utilizing $\mathcal{H}_\infty$ control with nominal values of any parameters. Control objectives are introduced using weighting functions over particular closed-loop transfer functions [48]. After that, an extended model including these weighting functions is obtained. An optimal controller can now be computed using the control tools included with the MATLAB® software environment. A multi-variable $\mathcal{H}_\infty$ controller is classically obtained, ensuring that all desired control objectives are satisfied. If such a controller cannot be obtained in the first step, the choice of weighting functions should be reviewed. The controller is then redesigned using the new weighting functions. For the validation of controller design, closed-loop time-domain simulations using averaged or topological models are convenient;
- Finally, a robustness analysis, in which uncertainty models are incorporated to account for parametric uncertainties or unmodeled dynamics, is carried out to assess the desired $\mathcal{H}_\infty$ controller robustness. If this condition is not met, the control objectives must be modified and Step 3 must be re-performed.

As a generic approach, closed-loop time-domain simulations performed with MATLAB® / Simulink® using topological and averaged modelling methodologies is employed in this work to validate the desired controller performance and robustness.

IV. DYNAMIC SPECIFICATIONS

When high penetration of renewables is aimed at, especially in stand-alone operation, frequency variations can lead to global instabilities [42], [49]. Properly conceived ESSs may then help at maintaining the stability and/or improving the MG frequency transient response by instantaneous active power absorption or injection in response to disturbances. In the MG in Fig. 1(a), primary frequency regulation relies upon participation of both the ESS (the supercapacitor in this case) and the classical source (the diesel generator), where the task assigned to the former is a faster recovery of the MG frequency, f_{grid}, in response to either load or production power variation.

Thus, dynamic performance of the frequency response – overshoot, response time, steady-state error – is imposed by the grid codes, whose requirements may slightly vary in different countries or regions [50], [51]. These grid codes can be pertinently "translated" based on the time-domain response in the case where only the classical source partic-

ipates in primary control – in this way, a template of the MG small-signal frequency deviation can result, like shown in Fig. 6 or Fig. 7(a). Regulation of the DC-bus voltage V_{dc} at a reference value V_{dc}^{ref} – in this case, 150 V – adds extra dynamic performance. Thus, secure and reliable operation of the DC-bus capacitor is guaranteed (e.g., this chemical capacitor can withstand a maximum voltage of 250 V). Note that in this case it is not about some stiff grid codes to be met, but just to define some suitable performance specification like, for example, indicated in Fig. 7(b) [47], [52].

Time-domain templates in Figs. 7(a) and 7(b) are important, as they further help at deducing the corresponding templates in the frequency domain – namely, in the form and parameters of the weighting functions – coherently with the $\mathcal{H}_\infty$ control design.

V. SYSTEM MODELLING FOR $\mathcal{H}_\infty$ CONTROL

The electrical circuit diagram of the approached ESS is depicted in Fig. 8. The power-electronic converters are represented by their equivalent linearized averaged models [40]. Concerning power generation units, taking into account their high-order, possibly multi-scale nature, per-unit modelling is preferred for its generally better numerical conditioning, thus being easier to handle by control design methods and improving numerical computation stability [53], [54]. Thus, a per-unitized model of the investigated ESS is further employed.

To ensure that the dynamic specifications specified in Section IV are fulfilled, a hierarchical control strategy consisting of two levels – namely cascaded two-level control structure – is designed and used in this work, where the outer control loop deals with output regulation imposing low-frequency dynamics (e.g., ΔV_{sc}, ΔV_{dc}, ΔP_{diesel}, Δf_{grid}) and the inner loop concerns current reference tracking of high-frequency dynamics (e.g., ΔI_s, ΔI_{rd}, ΔI_{rq}). This enables regulation of the output circuit while maintaining the internal variables within predetermined safety limits [55]. In addition, the $\mathcal{H}_\infty$-based upper-level multi-variable controller computes current references for the classical PI-based low-level controllers to track, enabling optimal rejection of load disturbances while meeting all dynamic performance and constraint criteria. This strategy is coherent with considering the power sources as current sources, as is the case with the majority of energy management systems and in accordance with control objectives [56], thus being preferable from an application viewpoint. Fig. 9 depicts the proposed global control structure [40]. The current control level is detailed in [40], [41], and [45], where PI controller coefficients are computed *via* identification based on the closed-loop transfer functions of the inner control loops. System modelling for $\mathcal{H}_\infty$ control loop is given in this section.

The current reference variations provided by the $\mathcal{H}_\infty$ controller are tracked with very fast dynamics by the inner loops; thus $\Delta I_s \equiv \Delta I_s^{ref}$ and $\Delta I_{rd} \equiv \Delta I_{rd}^{ref}$ from the viewpoint of the outer $\mathcal{H}_\infty$ loop. As the supercapacitor voltage, V_{sc}, is initially considered time invariant in the $\mathcal{H}_\infty$ design, then
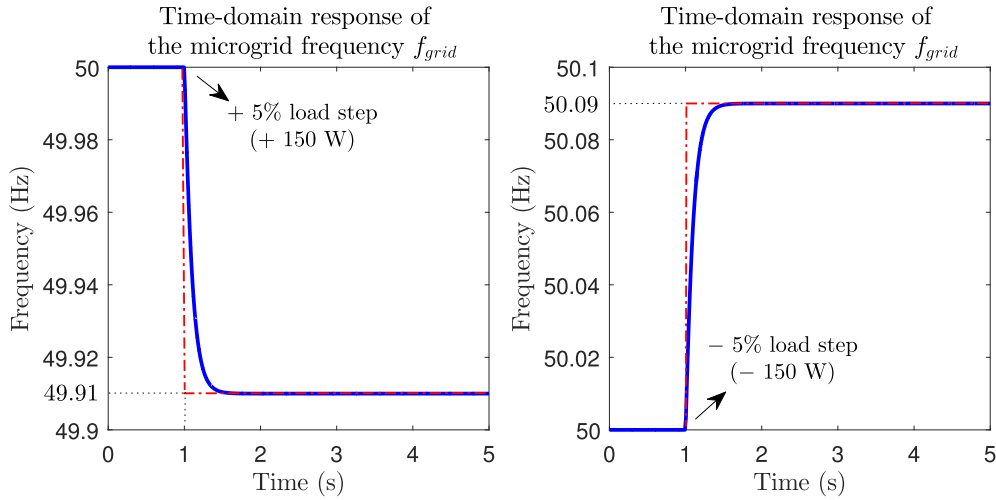
FIGURE 6. Performance specification on the MG frequency variation in response to a load step disturbance of ±5% of the load rated active power (±150 W) in the time domain [40].
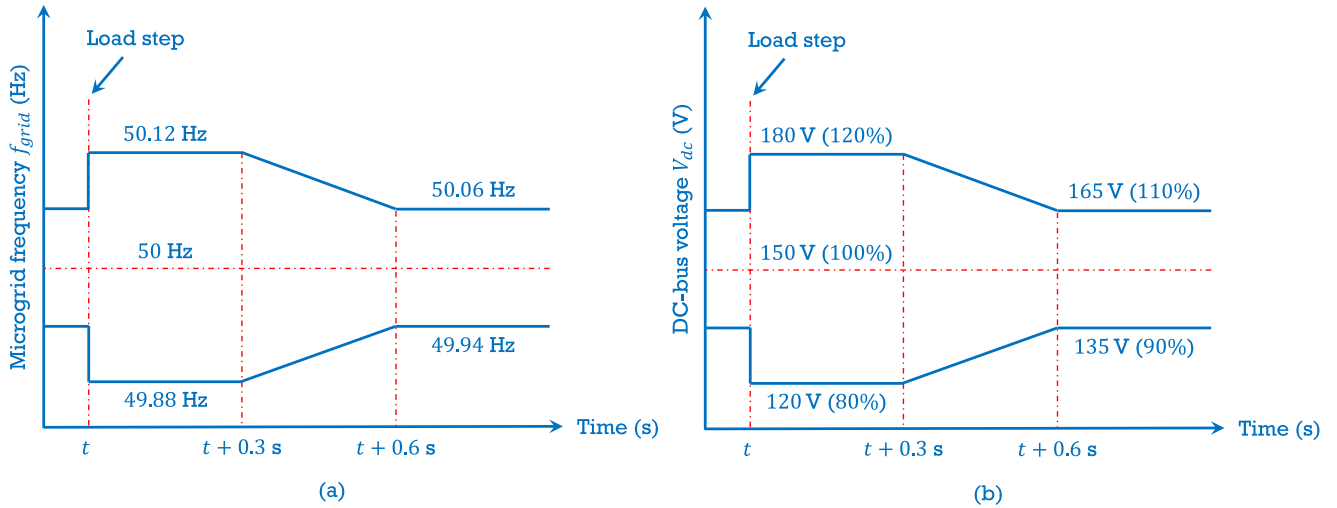

FIGURE 7. Grid code based performance specification on (a) the MG frequency variation [50], [51] and (b) the DC-bus voltage variation [40] in response to any load step disturbance in the time domain.
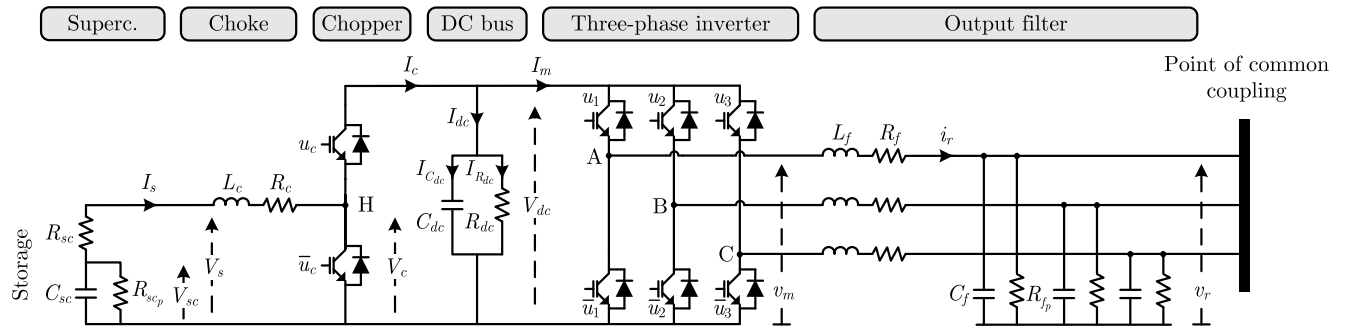

FIGURE 8. Schematic diagram of the supercapacitor-based ESS [40].

$\Delta V_{sc} = 0$ (its dynamic equation $\Delta \dot{V}_{sc} = f\left(\Delta V_{sc}, \Delta I_s\right)$ is disregarded). For the considered MG, the DC-side base

values result from the initial selection of the base values of AC-side variables, as detailed in Appendix C. By noting a
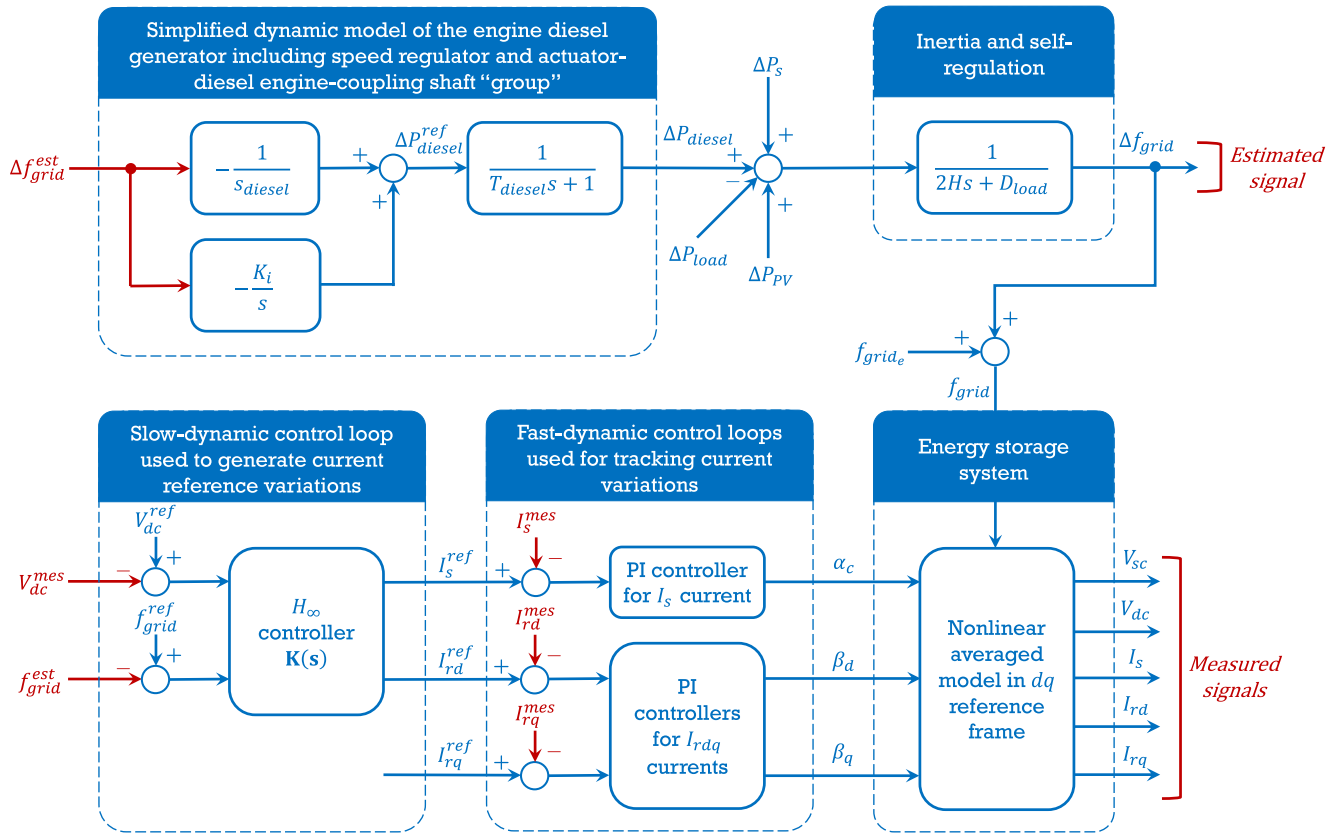
FIGURE 9. Block diagram of the proposed global control structure [40].

per-unitized value by the underline $\underline{X}$, the linear state-space per-unitized model of the studied MG, using the state variables shown in Fig. 8 and the Park coordinates transformation presented in Appendix D, can globally be expressed as (with $\underline{\Delta I_{rq}} \equiv \underline{\Delta I_{rq}^{ref}} = 0$) [40], [41], [45]

$$\begin{cases} \underline{\Delta \dot{x}} = \mathbf{A} \underline{\Delta x} + \mathbf{B_1} \underline{\Delta u} + \mathbf{B_2} \underline{\Delta w} \\ \underline{\Delta y} = \mathbf{C} \underline{\Delta x} + \mathbf{D_1} \underline{\Delta u} + \mathbf{D_2} \underline{\Delta w}, \end{cases} \tag{8}$$

with the state vector $\underline{\Delta x} = \begin{bmatrix} \Delta V_{dc} & \Delta P_{diesel} & \Delta f_{grid} \end{bmatrix}^T$ being constituted of the variations of the DC-bus voltage, of the diesel generator active power, and of the MG frequency. The control input vector $\underline{\Delta u} = \begin{bmatrix} \Delta I_s^{ref} & \Delta I_{rd}^{ref} \end{bmatrix}^T$ is made up of the supercapacitor output current reference variation and the d-component of the inverter output current reference variation. Because the PV source model – and presumably its control system – is not explicitly taken into account, $\underline{\Delta w} = \underline{\Delta P_{load}} - \underline{\Delta P_{PV}}$ behaves as an uncontrollable aggregated load variation – resulting from the combined action of load and PV active power variations – thus playing the role of a disturbance input. Hence, subjecting the system to PV power step changes will be representative of the most unfavourable case from a control viewpoint, given their theoretically infinite spectrum, compared to the band-limited solar irradiance spectrum. The measured variables are pooled

to generate the output vector $\underline{\Delta y} = \begin{bmatrix} \Delta V_{dc} & \Delta f_{grid} \end{bmatrix}^T$. The final identification of the matrices $\mathbf{A}$, $\mathbf{B_1}$, $\mathbf{B_2}$, $\mathbf{C}$, $\mathbf{D_1}$, and $\mathbf{D_2}$ in (8) is as follows

$$\mathbf{A} = \begin{bmatrix} -\dfrac{\omega_b}{R_{dc}C_{dc}} & 0 & 0 \\ 0 & -\dfrac{1}{T_{diesel}} & -\dfrac{1}{T_{diesel}s_{diesel}} \\ 0 & \dfrac{1}{2H} & -\dfrac{D_{load}}{2H} \end{bmatrix},$$

$$\mathbf{B_1} = \begin{bmatrix} \dfrac{\omega_b}{C_{dc}}\alpha_{c_e} & -\dfrac{\omega_b}{C_{dc}}\beta_{d_e} \\ 0 & 0 \\ \dfrac{1}{2\underline{H}}\left(\underline{V_{sc_e}} - 2R_{sc}\underline{I_{s_e}}\right) & 0 \end{bmatrix},$$

$$\mathbf{B_2} = \begin{bmatrix} 0 \\ 0 \\ -\dfrac{1}{2H} \end{bmatrix}, \quad \mathbf{C} = \begin{bmatrix} 1 & 0 & 0 \\ 0 & 0 & 1 \end{bmatrix},$$

$$\mathbf{D_1} = \begin{bmatrix} 0 & 0 \\ 0 & 0 \end{bmatrix}, \quad \mathbf{D_2} = \begin{bmatrix} 0 \\ 0 \end{bmatrix},$$

where chopper PWM duty cycle is denoted by α_c, β_d and β_q are the d- and q-components of the inverter switching function average value, respectively, whereas $\underline{\omega_{grid}}$ and ω_b are the

TABLE 1. Steady-state real-unit values of the linearized system represented by the laboratory prototype.

Variable	$V_{sc_e} \approx V_{s_e}$	V_{dc_e}	V_{rd_e}	V_{rq_e}
Value	48 V	150 V	80 V	0 V
Variable	I_{s_e}	I_{rd_e}	I_{rq_e}	α_{c_e}
Value	-0.033 A	-0.239 A	0 A	0.32
Variable	β_{d_e}	β_{q_e}	f_{grid_e}	
Value	0.533	-0.0035	50 Hz	
Variable	P_{s_e}	P_{diesel_e}	P_{PV_e}	P_{load_e}
	$\approx 20\%$ PV penetration			
Value	-0.0016 kW	2.5016 kW	0.5 kW	3 kW
	$\approx 50\%$ PV penetration			
Value	-0.0016 kW	2.0016 kW	1 kW	3 kW
	$\approx 100\%$ PV penetration			
Value	-0.0016 kW	1.5016 kW	1.5 kW	3 kW

MG pulsation and pulsation base unit, respectively. Subscript e indicates the steady-state operating point. Table 1 displays the steady-state real-unit values of the linearized system as reflected by the laboratory prototype whose parameter values are reported in Appendix B. For $\mathcal{H}_\infty$ control design, note that the selected steady-state value of the supercapacitor voltage V_{sc_e} corresponds to the maximum supercapacitor voltage, i.e., $V_{sc_e} = V_{sc_{max}} = 48$ V, implying that the supercapacitor is fully charged prior to testing. The aim is to prevent the PWM duty cycle of the chopper α_c from reaching its saturation threshold in case of large load disturbances. Indeed, since the chopper duty cycle α_c is directly proportional to the supercapacitor voltage V_{sc}, a large load variation may result in a dramatic decrease in V_{sc}, which rapidly drives α_c to its practical limits (i.e., $\alpha_c \in [0.1, 0.9]$).

VI. $\mathcal{H}_\infty$ CONTROL DESIGN

In order to deal with uncertainties of the system under consideration, the multi-variable control problem is stated in an optimal and robust control framework, namely in the $\mathcal{H}_\infty$ formalism, as suggested by block diagram in Fig. 10, which is the result of particularizing the general control structure in [48]. Typically, the S/KS mixed-sensitivity optimization problem is a disturbance rejection problem; in this case, the d- and q-components of load and PV output currents' variations are classified as disturbances [48]. Effective design requires judicious selection of the weighting functions $W_{perf}(s)$ to describe the disturbance rejection objective and $W_u(s)$ to account for the limits imposed on the control inputs.

The generalized plant **P** has three inputs, namely, the active power variation $\Delta P_{load} - \Delta P_{PV}$ acting as a disturbance input $\Delta \mathbf{w}$ and the current reference variations ΔI_s^{ref}, ΔI_{rd}^{ref}, which are the control inputs $\Delta \mathbf{u}$. The measured output vector $\Delta \mathbf{y}$ is composed of the DC-bus voltage variation ΔV_{dc} and the MG frequency variation Δf_{grid}. The desired performances are expressed in the form of weighting functions on the chosen performance outputs. ΔV_{dc}, Δf_{grid}, as well as ΔI_s^{ref}, ΔI_{rd}^{ref}, are chosen as performance outputs. Its vector is noted $\Delta \mathbf{z}$ in Fig. 10.

The DC-bus voltage variation ΔV_{dc} and the MG frequency variation Δf_{grid} are bounded by first-order linear time-invariant weighting functions $W_{perf}(s)$ of the following

TABLE 2. Weighting function parameters $W_{perf}(s)$ [40], [57].

	ΔV_{dc}	Δf_{grid}
M_s	$\dfrac{0.05 V_{dc_e}}{0.05 P_{load_e}}$	$\dfrac{(50.08 - f_{grid_e})/f_b}{0.05 P_{load_e}}$
A_ε	$\dfrac{0.025 V_{dc_e}}{0.05 P_{load_e}}$	$\dfrac{(50.04 - f_{grid_e})/f_b}{0.05 P_{load_e}}$
ω_b	$\dfrac{1}{240 T_{0_{rdq}}} \ (t_{r_1} \approx 0.6s)$	$\dfrac{1}{240 T_{0_{rdq}}} \ (t_{r_2} \approx 0.6s)$

TABLE 3. Weighting function parameters $W_u(s)$ [40], [57].

	ΔI_s^{ref}	ΔI_{rd}^{ref}
M_u	$\dfrac{I_{s_{max}} - I_{s_e}}{0.05 P_{load_e}}$	$\dfrac{I_{rd_{max}} - I_{rd_e}}{0.05 P_{load_e}}$
A_u	$0.1 M_u$	$0.1 M_u$
ω_{bc}	$\dfrac{1}{400 T_{PWM_c}}$	$\dfrac{1}{400 T_{PWM_i}}$

form [40], [48], [57]

$$\frac{1}{W_{perf}(s)} = \frac{s + \omega_b A_\varepsilon}{s/M_s + \omega_b}. \tag{9}$$

The function $1/W_{perf}(s)$ can be representative of time-domain response specifications, where the high-frequency gain M_s has an influence on the system overshoot, whereas the cut-off frequency ω_b tunes the desired response time and the low-frequency gain A_ε allows limiting the steady-state error [52].

The active power injection or absorption of the ESS is controlled *via* I_s. The DC-bus voltage is regulated *via* I_{rd}. Thus, the supercapacitor output current reference variation ΔI_s^{ref} and the direct component of the inverter output current reference variation ΔI_{rd}^{ref} are bounded by first-order linear time-invariant weighting functions $W_u(s)$ written as follows [40], [48], [57]

$$\frac{1}{W_u(s)} = \frac{A_u s + \omega_{bc}}{s + \omega_{bc}/M_u}. \tag{10}$$

The parameters of the weighting functions $W_{perf}(s)$ and $W_u(s)$ are listed in Tables 2 and 3, respectively [40], [57]. $1/T_{0_s}$ and $1/T_{0_{rdq}}$ denote the ΔI_s and ΔI_{rdq} inner imposed closed-loop bandwidths, respectively. $T_{PWM_c} = 1/f_{PWM_c}$ and $T_{PWM_i} = 1/f_{PWM_i}$, where f_{PWM_c} and f_{PWM_i} are the PWM switching frequency of the chopper and the PWM switching frequency of the three-phase inverter, respectively.

According to the system modelling and the selected weighting functions, a full-order $\mathcal{H}_\infty$ controller is designed using MATLAB® Robust Control Toolbox. The obtained result corresponds to the minimization of the norm [48]

$$\left\| \begin{matrix} W_{perf} S \\ W_u KS \end{matrix} \right\|_\infty < \gamma, \tag{11}$$

with $S(s)$ and $KS(s)$ being the sensitivity function and complementary sensitivity function, respectively. The function $S(s)$ describes the behavior of the output signal y, while $KS(s)$ describes the behavior of the control signal u following an output disturbance d_y.
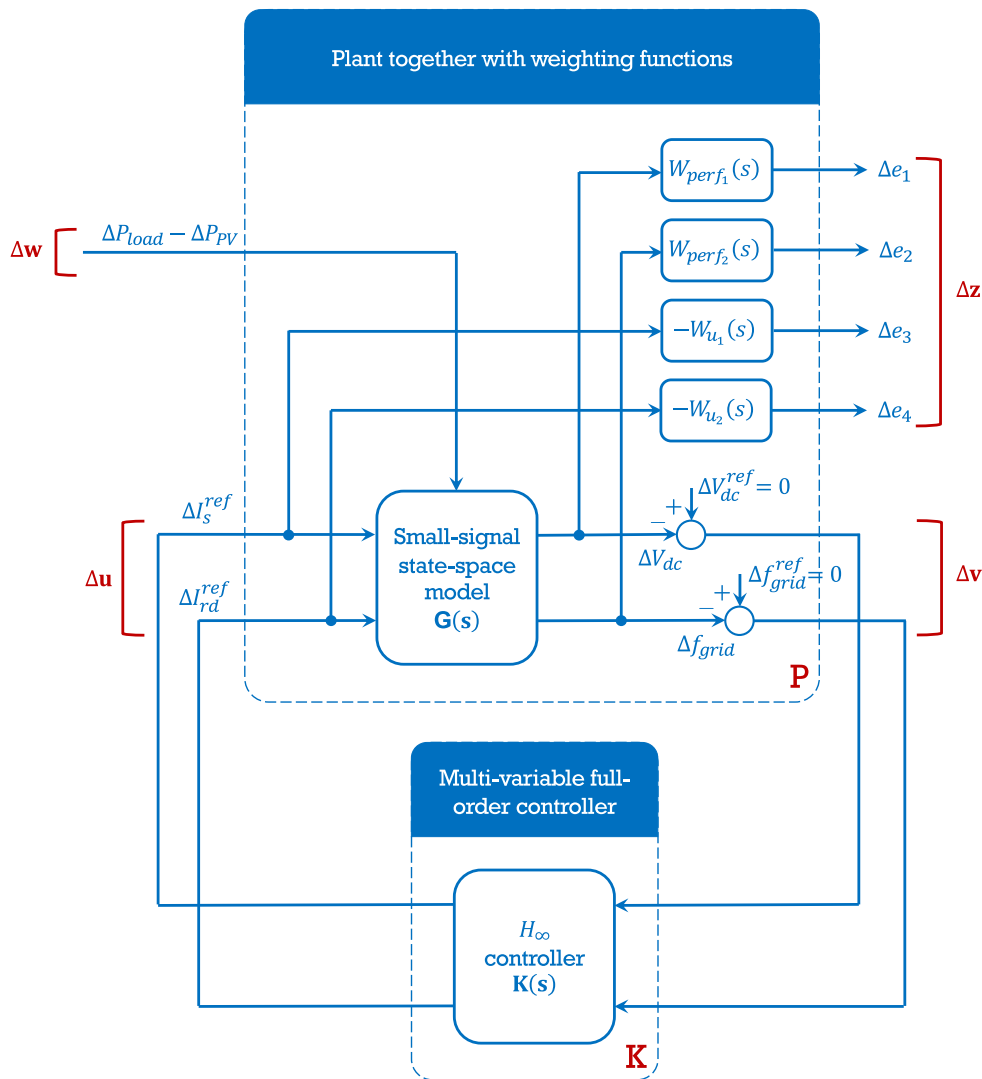
FIGURE 10. Control configuration in the so-called $P - K$ form, where **P** denotes the plant together with the weighting functions and K denotes the $\mathcal{H}_\infty$ controller [40].

Utilizing MATLAB® Robust Control Toolbox for numerical computation, a solution for the relevant LMIs is obtained after seven iterations, in the form of a multi-variable eighth-order $\mathcal{H}_\infty$ controller with an optimal value $\gamma = 1.014$ and an $\mathcal{H}_\infty$ norm $= 0.584$. This optimization quality enables the computed $\mathcal{H}_\infty$ controller to provide stable and robust performance in response to a load or PV power step of $\pm 5\%$ of P_{load_e} (i.e., ± 150 W) delivered to the system, as shown in the following section.

The LMIs involve matrices of the state-space model computed in the considered operating (equilibrium) point (numerical equilibrium values are given in Table 1), therefore a single operating point is concerned in the design. This operating point is further taken as "nominal". If this operating point changes, then matrices involved in the LMIs change also, another optimization problem is then solved. The goal of the robustness analysis performed in the next section is to show

whether the "nominal" controller still performs as imposed, despite variations of one of the parameters – that is, the super-capacitor state of charge – in relation to its "nominal" value. In addition, compared to an LPV/$\mathcal{H}_\infty$ control problem being treated off-line by solving a set of LMIs using Yalmip/Sedumi solver (convex optimization using single Lyapunov function, i.e., quadratic stabilization) at each vertices of the polytope [56], the established $\mathcal{H}_\infty$ robust control optimization approach is formulated with a mixed sensitivity problem by properly selecting weighting functions with a simple solution to the convex LMI condition.

In summary, the systematic procedure for $\mathcal{H}_\infty$ control design can be carried out following steps depicted in Fig. 11.

VII. NUMERICAL SIMULATION RESULTS
To demonstrate the validity and effectiveness of the proposed frequency robust control approach, a series of
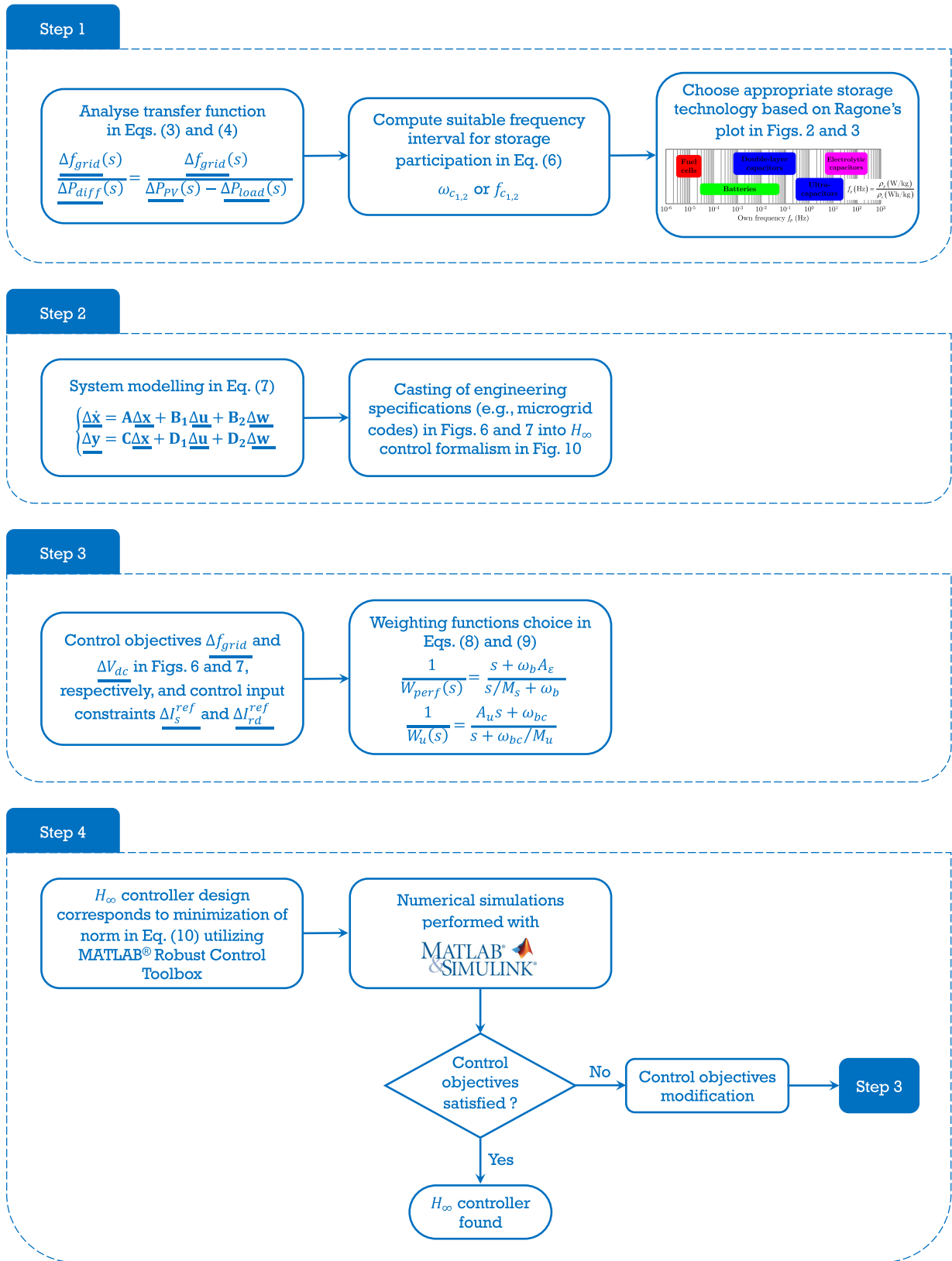
Step 1

Analyse transfer function
in Eqs. (3) and (4)

$$\frac{\Delta f_{grid}(s)}{\Delta P_{diff}(s)} = \frac{\Delta f_{grid}(s)}{\Delta P_{PV}(s) - \Delta P_{load}(s)}$$

Compute suitable frequency
interval for storage
participation in Eq. (6)

$$\omega_{c_{1,2}} \text{ or } f_{c_{1,2}}$$

Choose appropriate storage
technology based on Ragone's
plot in Figs. 2 and 3

Step 2

System modelling in Eq. (7)

$$\begin{cases} \Delta \dot{\mathbf{x}} = \mathbf{A}\Delta\mathbf{x} + \mathbf{B_1}\Delta\mathbf{u} + \mathbf{B_2}\Delta\mathbf{w} \\ \Delta\mathbf{y} = \mathbf{C}\Delta\mathbf{x} + \mathbf{D_1}\Delta\mathbf{u} + \mathbf{D_2}\Delta\mathbf{w} \end{cases}$$

Casting of engineering
specifications (e.g., microgrid
codes) in Figs. 6 and 7 into H_∞
control formalism in Fig. 10

Step 3

Control objectives Δf_{grid} and
ΔV_{dc} in Figs. 6 and 7,
respectively, and control input
constraints ΔI_s^{ref} and ΔI_{rd}^{ref}

Weighting functions choice in
Eqs. (8) and (9)

$$\frac{1}{W_{perf}(s)} = \frac{s + \omega_b A_\varepsilon}{s/M_s + \omega_b}$$

$$\frac{1}{W_u(s)} = \frac{A_u s + \omega_{bc}}{s + \omega_{bc}/M_u}$$

Step 4

H_∞ controller design
corresponds to minimization of
norm in Eq. (10) utilizing
MATLAB® Robust Control
Toolbox

Numerical simulations
performed with

MATLAB®
&SIMULINK®

Control
objects
satisfied ? — No → Control objectives
modification → **Step 3**

Yes

H_∞ controller
found

FIGURE 11. Flowchart for the illustration of $\mathcal{H}_\infty$ control design procedure [40].
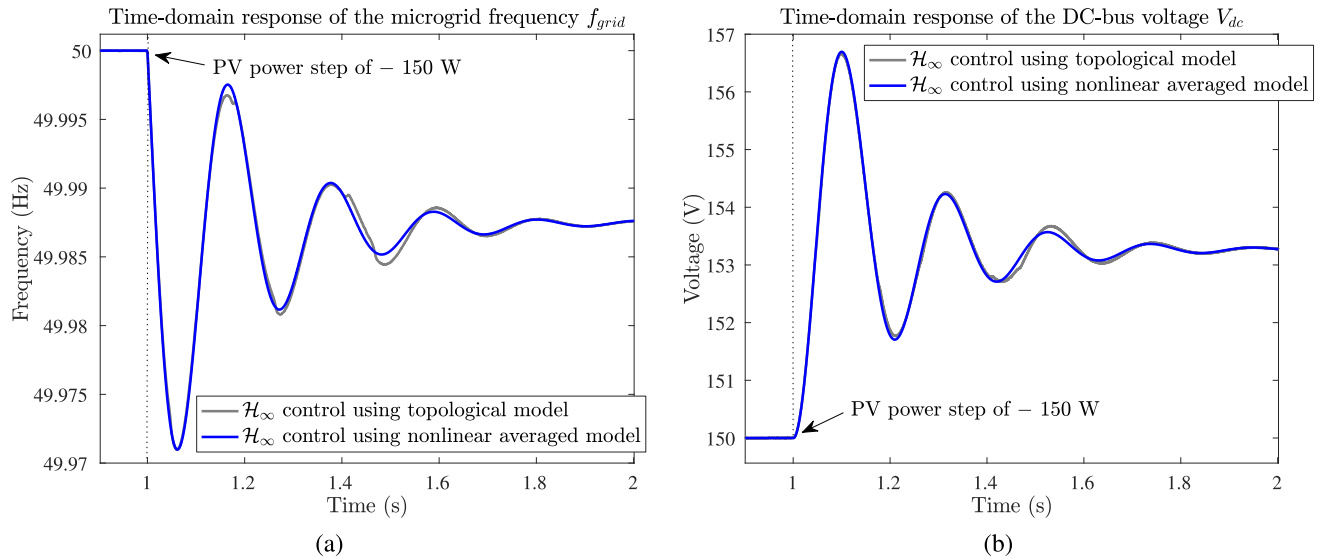
FIGURE 12. (a) MG frequency time-domain response f_{grid} and (b) DC-bus voltage time-domain response V_{dc} under a small PV power step disturbance of -5% of the load rated active power (-150 W) with respect to the rated operating point.

MATLAB®/Simulink® closed-loop time-domain simulations are performed on the topological model and the nonlinear averaged model. The topological model refers to the complete model of the ESS considering the ideal PWM switching functions of the chopper and the three-phase inverter as control inputs. Without sacrificing generality, load and PV device have here been considered as unknown *a priori* variable power levels and modelled as disturbances that must be rejected. PV power step changes ranging from -5% to -20% of the load rated active power P_{load_e} (i.e., from -150 W to -600 W) at $t = 1$ s are applied as disturbances. The supercapacitor voltage V_{sc}, which was initially viewed as a time-invariant parameter during the $\mathcal{H}_\infty$ controller synthesis, now appears as a time-variant parameter (i.e., $\Delta V_{sc} \neq 0$, its dynamic equation $\dot{V}_{sc} = f(V_{sc}, I_s)$ is accounted for in simulation models) in order to bring the physical representativeness of these models closer to reality.

A. MODEL VALIDATION AND EFFECTIVENESS OF THE PROPOSED ROBUST CONTROL STRATEGY

First, simulation results under a small PV power step disturbance of -5% of the load rated active power (-150 W) are presented and discussed.

In Figs. 12(a) and 12(b), the time-domain responses of the MG frequency f_{grid} and the DC-bus voltage V_{dc} are compared using topological and nonlinear averaged modelling, respectively. The results indicate good agreement between these models in the sense that the nonlinear averaged model – which is typically used for control purposes – closely approximates the converter's low-frequency behavior. Consequently, the nonlinear averaged model itself is validated when compared to the results of the topological model. Fig. 12(a) demonstrates that the MG frequency imposed time-domain performances are successfully achieved with respect to the

choice of the weighting function $W_{perf_2}(s)$ (i.e., a maximum overshoot of 0.08 Hz, a response time of roughly 0.6 s, and an acceptable steady-state error of 0.04 Hz). Compared to the case depicted in Fig. 6 in which only the diesel engine generator participates in primary frequency control, the storage device participation has considerably improved the dynamic performances of the MG frequency (i.e., lower overshoot, faster response time, and smaller steady-state error). In addition, the system is always stable. Fig. 12(b) shows that the DC-bus voltage imposed time-domain performances corresponding to the tuning of the weighting function $W_{perf_1}(s)$ are satisfied (i.e., a maximum overshoot of 7.5 V, a response time of approximately 0.6 s, and an allowable steady-state error of 3.75 V). Hence, the designed $\mathcal{H}_\infty$ controller meets the imposed dynamic performance requirements.

Figs. 13(a) and 13(b) respectively illustrate the time-domain responses of the supercapacitor output current I_s and the d-component of the inverter output current I_{rd} obtained with the nonlinear averaged model. It can be seen that the admissible limit is guaranteed for these currents with respect to the choice of the weighting functions $W_u(s)$, indicating that their imposed dynamic performance specifications are met.

Without sacrificing generality and for the sake of simplicity, the nonlinear averaged model is used for time-domain simulations going forward.

As demonstrated in Fig. 14, the ESS participation in primary frequency control has reduced the active power variation of the diesel engine generator. In addition, it should be noted that the load active power variation $\Delta P_{load} = 0$ does not reduce generality, as these variations may always be included in the aggregated static load. In this $\mathcal{H}_\infty$ robust control approach, it is evident that the primary control is mainly realized by the storage device, whereas there is only a slight change in the active power of the diesel generator
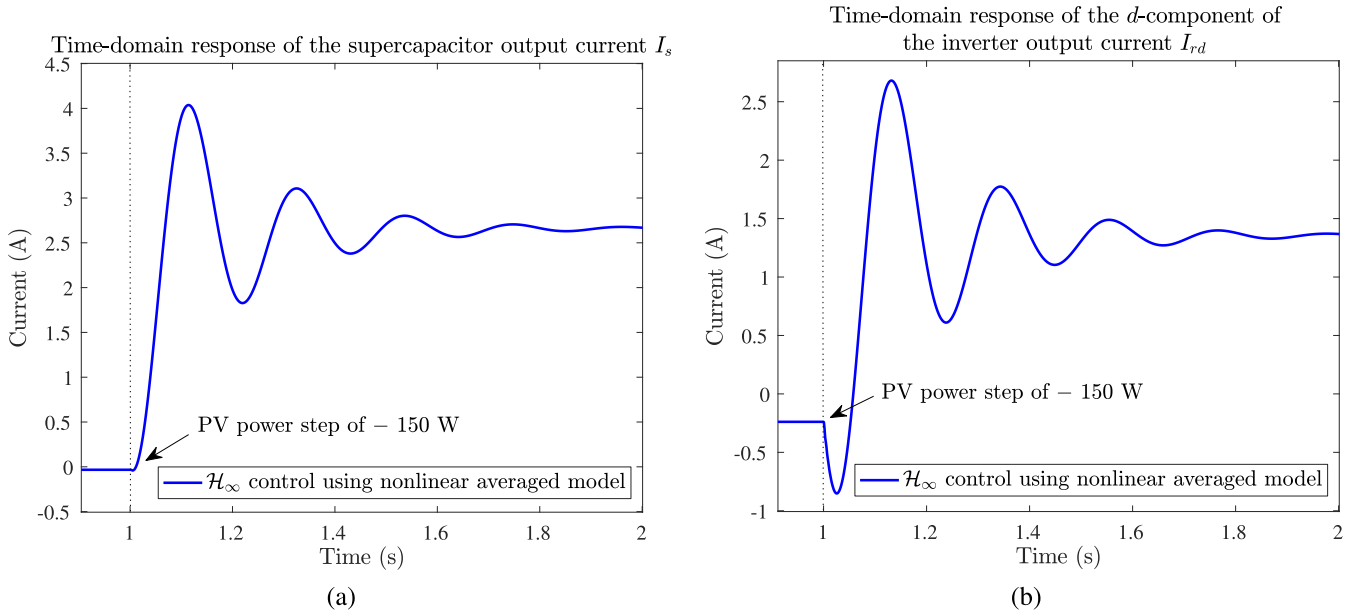
FIGURE 13. Time-domain responses of (a) the supercapacitor output current I_S and (b) the d-component of the inverter output current I_{rd} under a small PV power step disturbance of −5% of the load rated active power (−150 W) with respect to the rated operating point.
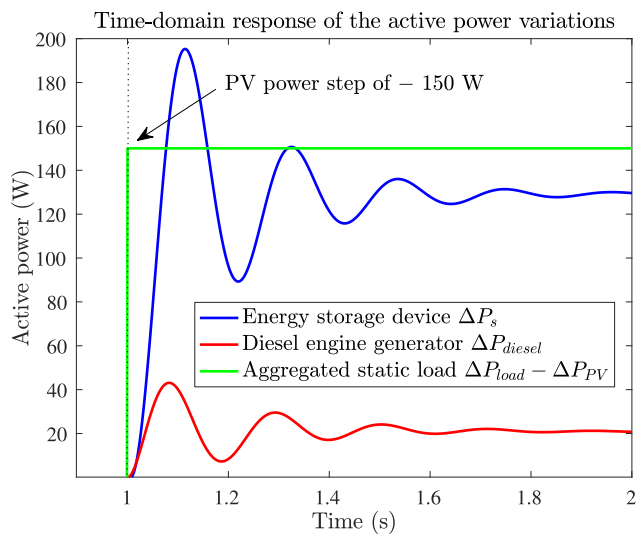

FIGURE 14. Active power variations of the sources and load under a small PV power step disturbance of −5% of the load rated active power (−150 W) with respect to the rated operating point.

during this time interval, allowing for the diesel generator to operate optimally around its steady-state operating point.

These results allow us to revisit the storage device initial choice and sizing. From the time-domain response of the active power variation of the storage device, its sizing can be defined from the maximum active power variation of the load or PV energy source. Then, if a small variation in the MG transient frequency is required, the storage device must provide a significant peak of power. The MG permissible frequency variation and the rated power of the storage device must be compromised. As the MG frequency

variation with the ESS by $\mathcal{H}_\infty$ control is fixed by the definition of the weighting function $W_{perf_2}(s)$, the imposed dynamic performance requirements should be relaxed so as to increase the MG admissible frequency variation, resulting in a reduction in power, energy, and thus the cost used by the storage device. For instance, the imposed steady-state value of the MG frequency can be increased from 0.04 Hz to 0.06 Hz (closer to the MG frequency time-domain response without ESS) to reduce the power supplied by the storage device. The required dynamic performances for the MG frequency variation are exclusively focused on primary frequency control. Consequently, the ESS is not involved in secondary frequency control. If the ESS is to participate in secondary frequency control, the MG frequency variation weighting function $W_{perf_2}(s)$ must be redesigned with a smaller steady-state value of the MG frequency variation (i.e., a smaller A_{ε_2}). In this case, nevertheless, a storage device with a higher energy density is required, which increases the investment cost [46].

In conclusion, under small PV power step disturbances of ±5% of the load rated active power (±150 W), the proposed frequency robust control approach has been shown to be effective, with the designed $\mathcal{H}_\infty$ controller capable of ensuring the required dynamic performances. In the following subsection, simulation results are presented and discussed for more demanding conditions involving larger PV power step changes as disturbances.

B. MORE STRESSED CONDITIONS
The previously designed PI and $\mathcal{H}_\infty$ controllers are now implemented in numerical simulations under larger PV power step variations ranging from −10% to −20% of the load rated
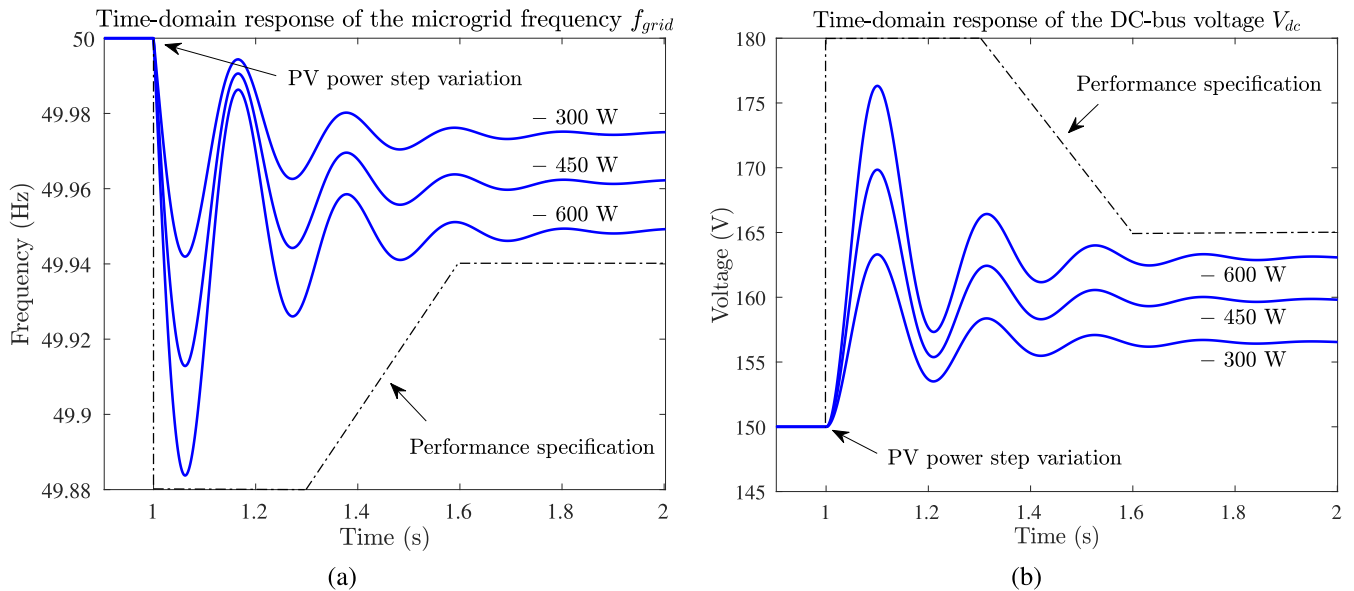
FIGURE 15. (a) MG frequency time-domain response f_{grid} and (b) DC-bus voltage time-domain response V_{dc} under PV power step disturbances ranging from −10% to −20% of the load rated active power (−300 W to −600 W) with respect to the rated operating point.
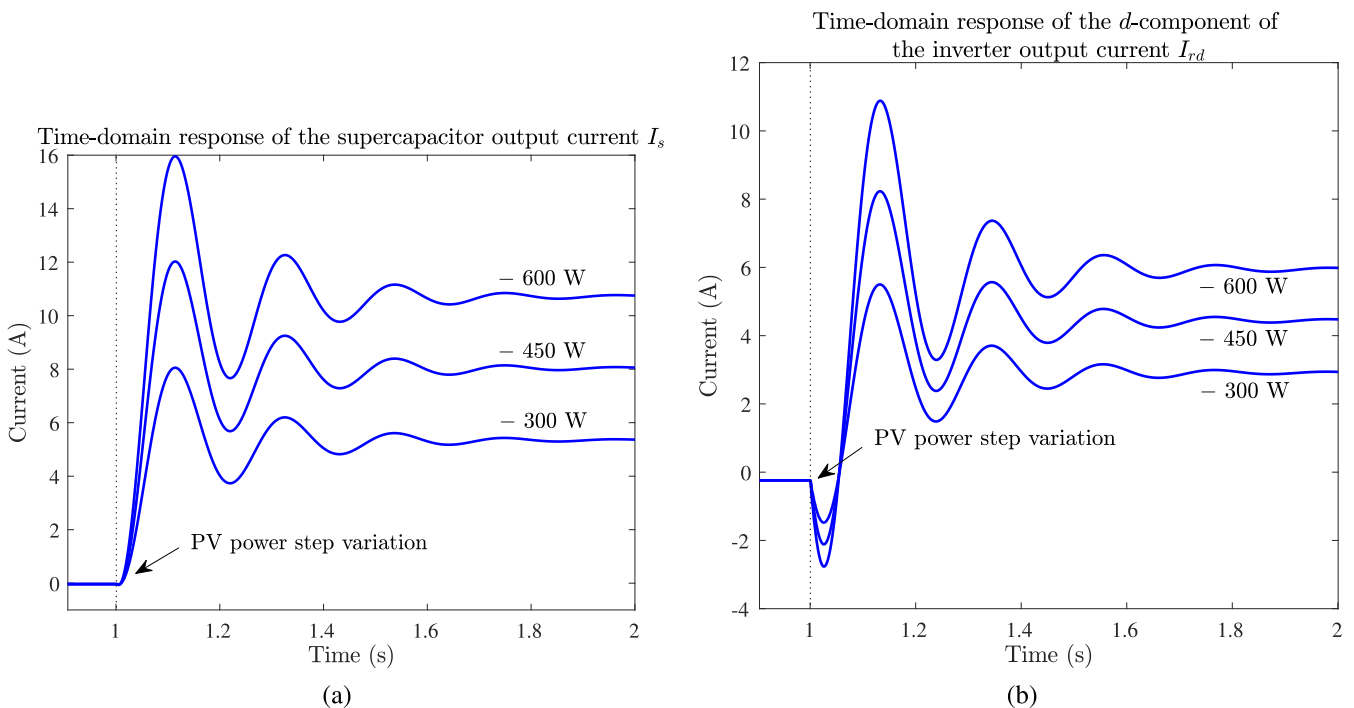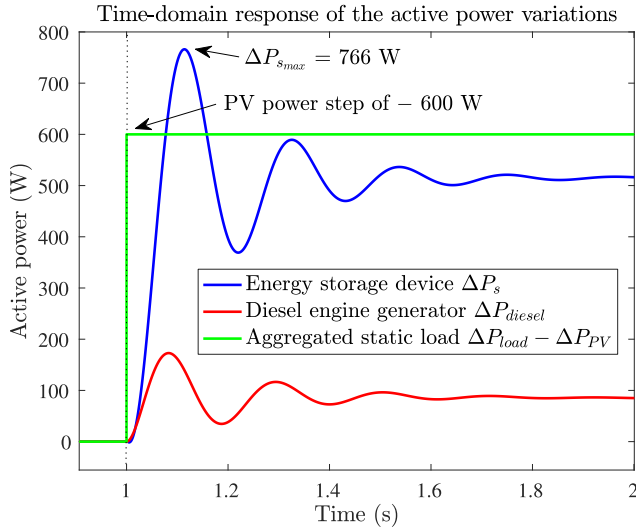

FIGURE 16. Time-domain responses of (a) the supercapacitor output current I_s and (b) the d-component of the inverter output current I_{rd} under PV power step disturbances ranging from −10% to −20% of the load rated active power (−300 W to −600 W) with respect to the rated operating point.

active power (i.e., from −300 W to −600 W). The idea is to more precisely evaluate the domain in which the implemented robust control ensures stable and robust performance.

Figs. 15(a) and 15(b) depict the time-domain responses of the MG frequency f_{grid} and the DC-bus voltage V_{dc}, respectively, obtained with the nonlinear averaged model. The $\mathcal{H}_\infty$ controller – designed with respect to the imposed

time-domain performances in the small-signal case (i.e., a variation of ±5% of the load rated active power, ±150 W) – can guarantee the performance specification of f_{grid} imposed in Fig. 7(a) (i.e., a maximum overshoot of 0.12 Hz, a response time of approximately 0.6 s, and an admissible steady-state error of 0.06 Hz, in response to any load active power step disturbances in the time domain), as represented in

FIGURE 17. Active power variations of the sources and load under a PV power step disturbance of −20% of the load rated active power (−600 W) with respect to the rated operating point.
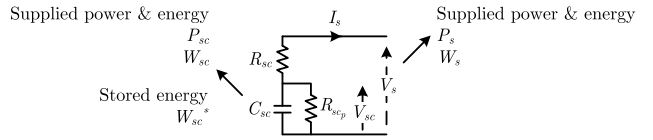

FIGURE 18. Schematic diagram of the supercapacitor.

viable solution for ensuring robust performance in the event of larger load or PV active power variations. In addition, variations of the steady-state operating point (e.g., changes in the steady-state value of the supercapacitor state of charge SoC_{sc_e} or voltage V_{sc_e}), the influence of parametric uncertainties, variations in system parameters, device aging, etc., should be analyzed to test the controller robustness.

C. UNCERTAINTY IN THE SUPERCAPACITOR STATE OF CHARGE SoC_{sc_e}

The diesel-PV-supercapacitor hybrid power generation system under investigation is susceptible to numerous sources of uncertainty. These uncertainties could initially be associated with system parameters. They may also represent the different dynamics of the real system that are neglected (not modeled) in the theoretical (mathematical) model or the model misinterpretation at high frequencies. Variations in the operating point (e.g., variability in PV system output power, variations in ESS capacity, etc.) could also be regarded as sources of uncertainty.

Typically, parametric uncertainties in the structured uncertainty class could be associated with the ESS parameters (i.e.; supercapacitor capacitor C_{sc}, series resistor R_{sc}, and parallel resistor R_{sc_p}; choke inductor L_c and resistor R_c; DC bus capacitor C_{dc} and resistor R_{dc}; output filter inductor L_f, capacitor C_f, series resistor R_f, and parallel resistor R_{f_p}), but they could also be representative of variations in the steady-state value of the supercapacitor state of charge SoC_{sc_e} (or supercapacitor voltage V_{sc_e}), which leads to changes in the steady-state operating point of the system. They could also represent changes in the MG equivalent inertia constant H and the load damping constant D_{load}. In addition, the time constant T_{diesel}, the droop value s_{diesel}, and the secondary control gain K_i of the diesel engine generator could be regarded as parametric uncertainties.

In this subsection, a robust performance analysis of the $\mathcal{H}_\infty$ controller, which was designed in the preceding section with the system parameters fixed at their rated values, is detailed. Initial consideration is given to the parametric uncertainty in the steady-state value of the supercapacitor state of charge SoC_{sc_e} (or supercapacitor voltage V_{sc_e}). Then, a robustness analysis is performed to determine whether or not the closed-loop system remains robust (from a performance point of view) to a given parametric uncertainty level in SoC_{sc_e} (or V_{sc_e}) around its design value, i.e., 48 V. Finally, MATLAB®/Simulink® closed-loop time-domain simulations are presented to validate the controller robustness and performance in the presence of multiple PV power step disturbances and uncertainty levels in SoC_{sc_e} (or V_{sc_e}).

Fig. 15(a). On the other hand, Fig. 15(b) demonstrates that the performance specification of V_{dc} imposed in Fig. 7(b) (i.e., a maximum overshoot at 20% of its rated value V_{dc_e}, 30 V, a response time of approximately 0.6 s, and an admissible steady-state error at 10% of V_{dc_e}, 15 V, in response to any load active power step disturbances in the time domain) are satisfied. The action domain of the $\mathcal{H}_\infty$ controller – computed with respect to the imposed weighting functions $W_{perf}(s)$ and $W_u(s)$ – thus ensures robust performance against variations of ±20% of the load rated active power (±600 W) around its steady-state operating point.

Figs. 16(a) and 16(b) respectively display the nonlinear-averaged-modelling-based time-domain responses of the supercapacitor output current I_s and the d-component of the inverter output current I_{rd}. It can be observed that the admissible limit is ensured for I_s and I_{rd} with respect to the choice of the weighting functions $W_u(s)$, which means that their imposed dynamic performance specifications are satisfied to variations of ±20% of the load rated active power (±600 W) around its steady-state operating point.

As demonstrated in Fig. 17, the maximum active power variation of the energy storage device is roughly equal to 766 W, i.e., $\Delta P_{s_{max}} = 766$ W or $P_{s_{max}} = 764$ W, as a result of the PV power step disturbance of −600 W. This value is less than its maximum possible active power of approximately 1500 W. In terms of secure and reliable operation, the ESS can thus provide active power demand caused by load or PV power step disturbances that are equal to ±20% of the load rated active power (±600 W) with respect to the rated operating point.

In short, the designed $\mathcal{H}_\infty$ controller guarantees stable and robust performance with variations of ±20% of the load rated active power (±600 W) around its steady-state operating point. Use of an LPV control strategy could be a

TABLE 4. Simulation results performed with PV power step disturbances ranging from −5% to −20% of the load rated active power (i.e., from −150 W to −600 W) while accounting for the uncertainty in V_{sc_e} (or SoC_{sc_e}).

PV power step disturbance ΔP_{PV}	$-5\% \, P_{load_e}$ $(-150\,\text{W})$	$-10\% \, P_{load_e}$ $(-300\,\text{W})$
Uncertainty in V_{sc_e}	[24, 48] V	[24, 48] V
Uncertainty in SoC_{sc_e}	[25, 100] %	[25, 100] %
Performance specification of f_{grid}	✓	✓
Uncertainty in V_{sc_e}	[24, 48] V	[24, 48] V
Uncertainty in SoC_{sc_e}	[25, 100] %	[25, 100] %
Performance specification of V_{dc}	✓	✓
PV power step disturbance ΔP_{PV}	$-15\% \, P_{load_e}$ $(-450\,\text{W})$	$-20\% \, P_{load_e}$ $(-600\,\text{W})$
Uncertainty in V_{sc_e}	[36, 48] V	48 V
Uncertainty in SoC_{sc_e}	[56, 100] %	100%
Performance specification of f_{grid}	✓	✓
Uncertainty in V_{sc_e}	[30, 48] V	[42, 48] V
Uncertainty in SoC_{sc_e}	[39, 100] %	[77, 100] %
Performance specification of V_{dc}	✓	✓

As a matter of fact, the estimation of SoC_{sc} is crucial for determining the optimal operating strategy of the ESS. SoC_{sc} can be approximated as the ratio between the stored energy W_{sc}^* depicted in Fig. 18 and the maximum storable energy $W_{sc_{max}}^*$ as follows (with the internal resistances R_{sc} and R_{sc_p} neglected)

$$SoC_{sc} = \frac{W_{sc}^*}{W_{sc_{max}}^*} = \frac{\frac{1}{2}C_{sc}V_{sc}^2}{\frac{1}{2}C_{sc}V_{sc_{max}}^2} = \left(\frac{V_{sc}}{V_{sc_{max}}}\right)^2, \quad (12)$$

where $V_{sc_{max}} = 48$ V is the maximum possible supercapacitor voltage. In practice, SoC_{sc} is kept within the allowable range of [25, 100] % to ensure reliable, efficient, and safe operation of the supercapacitor and to prolong its lifespan. The limited variation range, corroborated with (12), indicates that the V_{sc} value must be controlled between 24 V and 48 V. The maximum value, i.e., $V_{sc} = 48$ V, is a convenient choice for designing the nominal $\mathcal{H}_\infty$ controller whose robustness is further assessed.

Without sacrificing generality, MATLAB®/Simulink® nonlinear-averaged-modelling-based closed-loop time-domain simulations are performed with PV power step disturbances ranging from −5% to −20% of the load rated active power (i.e., from −150 W to −600 W) at $t = 1$ s. The supercapacitor voltage V_{sc} appears as a time-variant parameter (i.e., $\Delta V_{sc} \neq 0$) in the simulation model. In numerical simulations, the initial (steady-state) value of the supercapacitor state of charge SoC_{sc_e} ranges from 25% to 100%. Indeed, state of charge unbalance is caused by cells being charged to different state of charge levels. This in turn will result in a different open circuit voltage for cells and changes in the initial (steady-state) value of the supercapacitor voltage V_{sc_e}, leading to the initial values of some elements of the matrix $\mathbf{B_1}$ in (8) and the predefined steady-state operating point of this linearized system being changed.

Figs. 19 and 20 respectively depict the time-domain responses of the MG frequency f_{grid} and the DC-bus voltage V_{dc} while accounting for the uncertainty in V_{sc_e} (or

SoC_{sc_e}). Table 4 presents explicitly a number of noteworthy results illustrated in these two figures. It can be shown that the $\mathcal{H}_\infty$ controller – designed with respect to the imposed time-domain performances in the small-signal case (i.e., a variation of ±5% of the load rated active power, ±150 W) and computed with respect to the imposed weighting functions $W_{perf}(s)$ and $W_u(s)$ – can guarantee the performance specification of f_{grid} imposed in Fig. 7(a) (i.e., a maximum overshoot of 0.12 Hz, a response time of approximately 0.6 s, and an admissible steady-state error of 0.06 Hz, in response to any load active power step disturbances in the time domain) and the performance specification of V_{dc} imposed in Fig. 7(b) (i.e., a maximum overshoot at 20% of its rated value V_{dc_e}, 30 V, a response time of approximately 0.6 s, and an admissible steady-state error at 10% of V_{dc_e}, 15 V, in response to any load active power step disturbances in the time domain) against the entire variation range of $SoC_{sc_e} \in [25, 100]$ % (or $V_{sc_e} \in [24, 48]$ V) and caused by load or PV power step disturbances up to ±10% of the load rated active power (±300 W) relative to the rated operating point.

Figs. 21 and 22 display the time-domain responses of the supercapacitor output current I_s and the d-component of the inverter output current I_{rd}, respectively, while accounting for the uncertainty in V_{sc_e} (or SoC_{sc_e}). It can be observed that the admissible limit is maintained for I_s and I_{rd} with respect to the selection of the weighting functions $W_u(s)$, indicating that their imposed dynamic performance specifications are met to both simultaneous $SoC_{sc_e} \in [25, 100]$ % (or $V_{sc_e} \in [24, 48]$ V) and variations of ±20% of the load rated active power (±600 W) around its steady-state operating point.

As shown in Fig. 23, which depicts the time-domain response of the active power variation of the energy storage device ΔP_s under a PV power step disturbance of −20% of the load rated active power (−600 W) while accounting for the uncertainty in V_{sc_e} (or SoC_{sc_e}), the maximum active power variation of the ESS is always less than its maximum possible active power of roughly 1500 W, therefore the ESS can provide active power demand subject to $SoC_{sc_e} \in [25, 100]$ % (or $V_{sc_e} \in [24, 48]$ V) and caused by load or PV power step disturbances up to ±20% of the load rated active power (±600 W) relative to the rated operating point.

In summary, the synthesized $\mathcal{H}_\infty$ controller is robust in performance to $SoC_{sc_e} \in [25, 100]$ % (or $V_{sc_e} \in [390, 780]$ V) and with variations of ±10% of the load rated active power (±600 W) around its steady-state operating point. In the following subsection, the variation in the PV penetration rate ranging from $r_{PV} = 20\%$ to $r_{PV} = 100\%$ is accounted for, and the controller is redesigned and its robustness is re-tested to determine the control limitation.

D. HIGH PV PENETRATION RATE RANGING FROM $r_{PV} = 50\%$ TO $r_{PV} = 100\%$

Without loss of generality, MATLAB®/Simulink® closed-loop time-domain simulations on the basis of nonlinear averaged modelling are performed to validate the controller
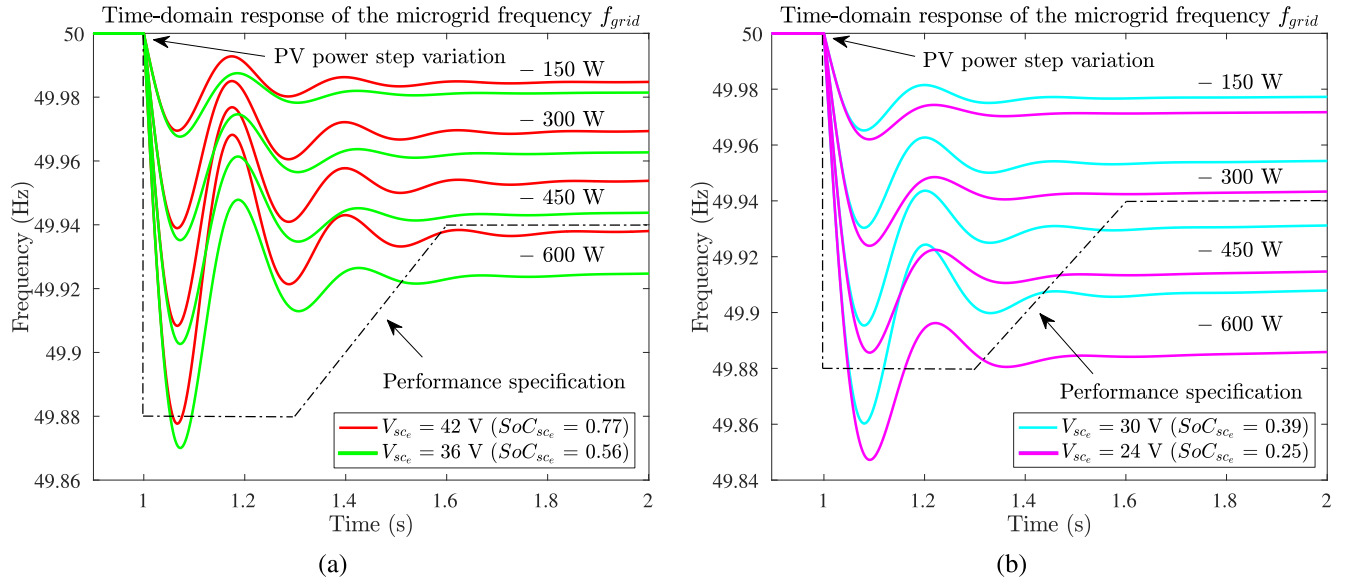
FIGURE 19. MG frequency time-domain response f_{grid} under PV power step disturbances ranging from -5% to -20% of the load rated active power (-150 W to -600 W) taking into account the uncertainty in V_{sc_e} (or SoC_{sc_e}).
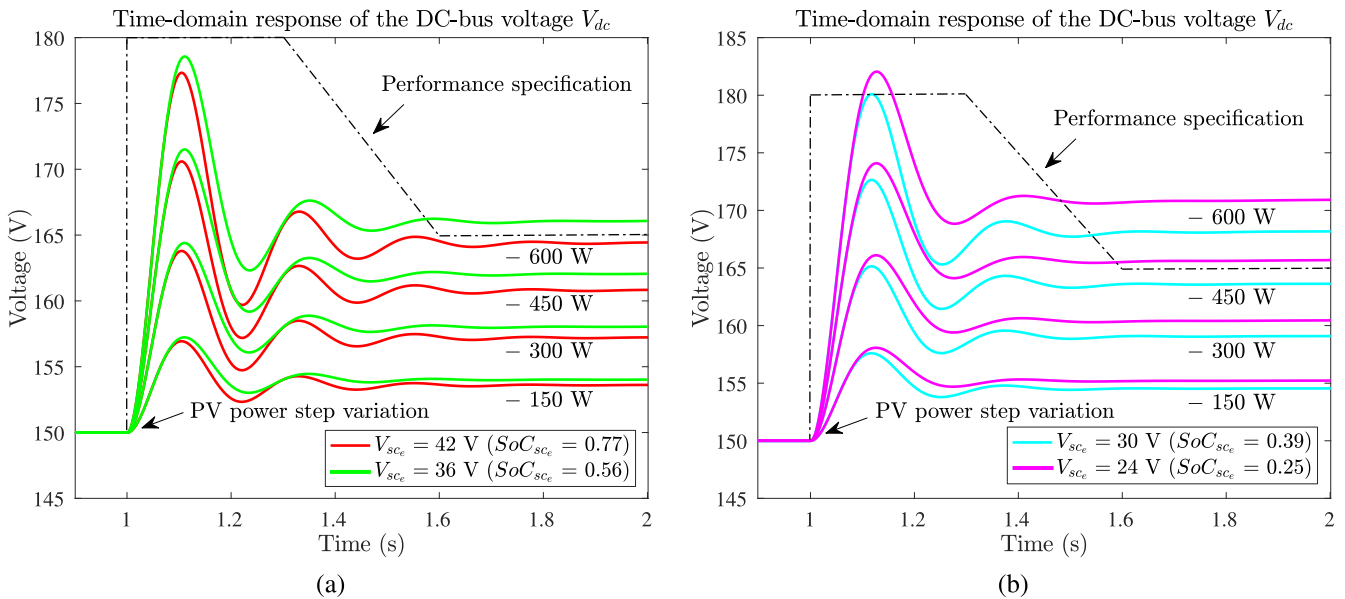

FIGURE 20. DC-bus voltage time-domain response V_{dc} under PV power step disturbances ranging from -5% to -20% of the load rated active power (-150 W to -600 W) taking into account the uncertainty in V_{sc_e} (or SoC_{sc_e}).

robustness and performance in the presence of multiple PV power step disturbances ranging from -5% to -20% of the load rated active power (i.e., from -150 W to -600 W) at $t = 1$ s and uncertainty levels in the PV penetration rate r_{PV} (resulting in considering the MG equivalent inertia constant $\underline{H}$ as a parametric uncertainty and thus the variation in the matrices of the state-space model (8) of the linearized system). The supercapacitor voltage V_{sc} appears as a time-variant parameter (i.e., $\Delta V_{sc} \neq 0$) in the simulation model. Let us assume that $r_{PV} \in [20, 100]\%$ corresponds to $\underline{H} \in [1, 0.6]$ in numerical simulations.

Figs. 24(a) and 24(b) depict the time-domain responses of the MG frequency f_{grid} and the DC-bus voltage V_{dc}, respectively, wherein three respective $\mathcal{H}_\infty$ controllers are designed with respect to three distinct scenarios in the PV penetration rate r_{PV} while accounting for the uncertainty the MG equivalent inertia constant $\underline{H}$. It can be shown that these $\mathcal{H}_\infty$ controllers – designed with respect to the imposed time-domain performances in the small-signal case (i.e., a variation of $\pm 5\%$ of the load rated active power, ± 150 W) and computed with respect to the imposed weighting functions $W_{perf}(s)$ and $W_u(s)$ – can guarantee the performance specification of f_{grid}
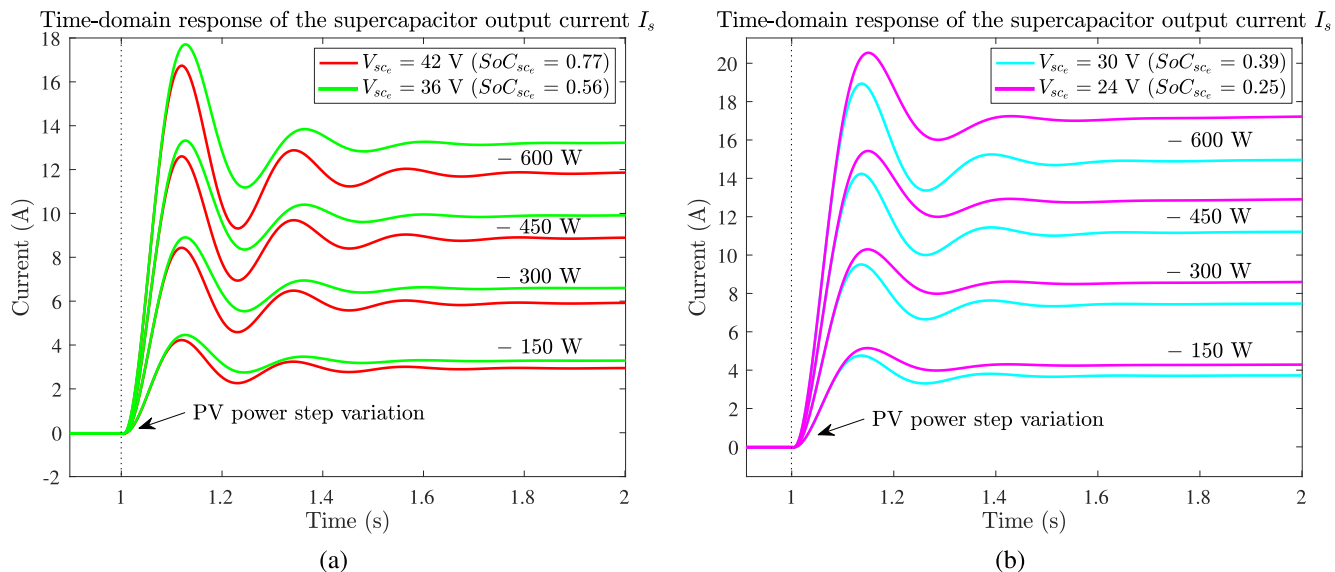
FIGURE 21. Time-domain response of the supercapacitor output current I_s under PV power step disturbances ranging from −5% to −20% of the load rated active power (−150 W to −600 W) taking into account the uncertainty in V_{sc_e} (or SoC_{sc_e}).
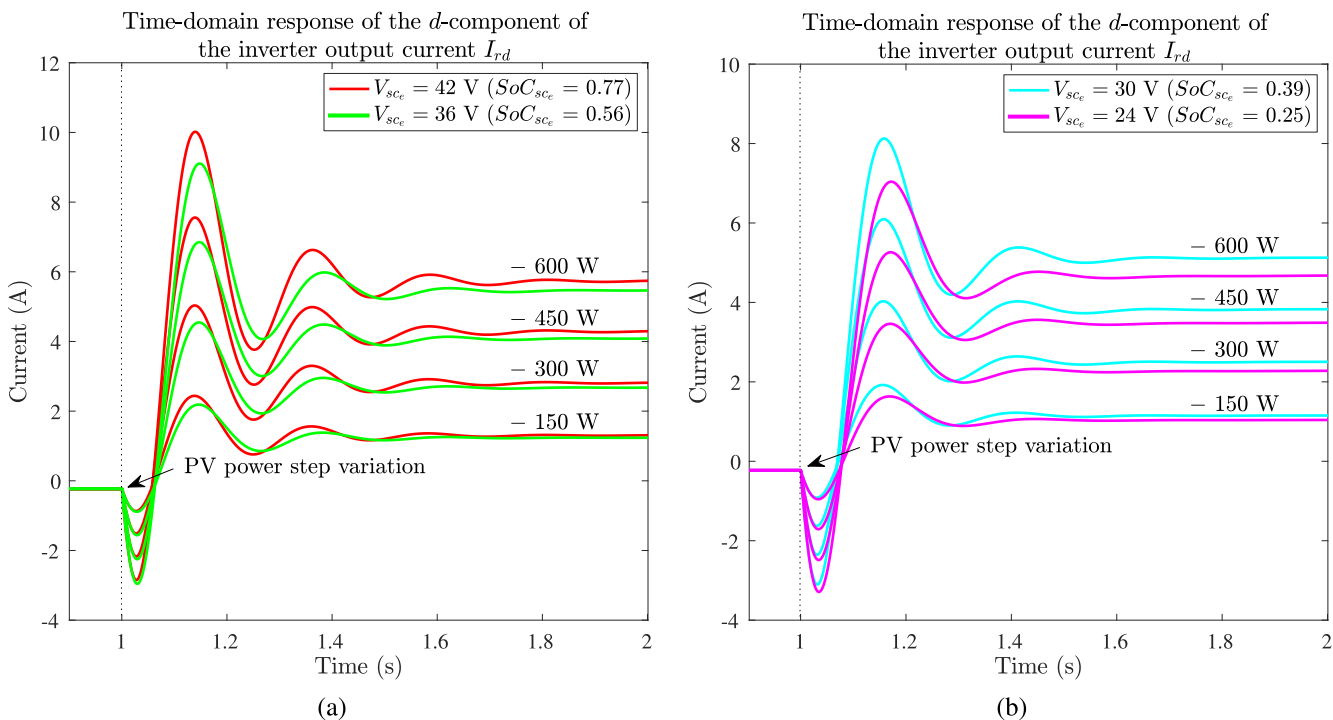

FIGURE 22. Time-domain response of the d-component of the inverter output current I_{rd} under PV power step disturbances ranging from −5% to −20% of the load rated active power (−150 W to −600 W) taking into account the uncertainty in V_{sc_e} (or SoC_{sc_e}).

imposed in Fig. 7(a) (i.e., a maximum overshoot of 0.12 Hz, a response time of approximately 0.6 s, and an admissible steady-state error of 0.06 Hz, in response to any load active power step disturbances in the time domain) and the performance specification of V_{dc} imposed in Fig. 7(b) (i.e., a maximum overshoot at 20% of its rated value V_{dc_e}, 30 V, a response time of approximately 0.6 s, and an admissible steady-state error at 10% of V_{dc_e}, 15 V, in response to any load active power step disturbances in the time domain) against the

entire variation range of $r_{PV} \in [20, 100]\%$ (or $\underline{H} \in [1, 0.6]$) and caused by load or PV power step disturbances up to ±15% of the load rated active power (±450 W) relative to the rated operating point.

Figs. 25(a) and 25(b) represent the time-domain responses of the supercapacitor output current I_s and the d-component of the inverter output current I_{rd}, respectively, with respect to three distinct scenarios in the PV penetration rate r_{PV} while accounting for the uncertainty the MG equivalent inertia
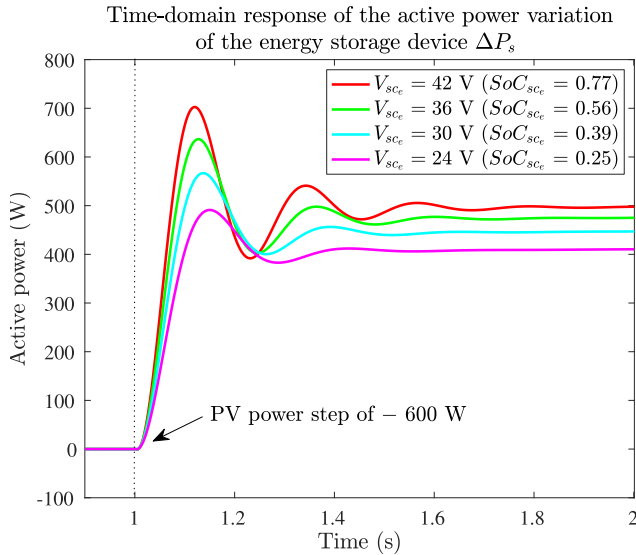
FIGURE 23. Active power variation of the energy storage device ΔP_s under a PV power step disturbance of -20% of the load rated active power (-600 W) taking into account the uncertainty in V_{sc_e} (or SoC_{sc_e}).

constant $\underline{H}$. It can be observed that the admissible limit is maintained for I_s and I_{rd} with respect to the selection of the weighting functions $W_u(s)$, indicating that their imposed dynamic performance specifications are met to both simultaneous $r_{PV} \in [20, 100]\%$ (or $\underline{H} \in [1, 0.6]$) and variations of $\pm 20\%$ of the load rated active power (± 600 W) around its steady-state operating point.

As depicted in Fig. 26, which illustrates the time-domain response of the active power variation of the energy storage device ΔP_s under a PV power step disturbance of -20% of the load rated active power (-600 W) with respect to three distinct scenarios in the PV penetration rate r_{PV} while accounting for the uncertainty the MG equivalent inertia constant $\underline{H}$, the maximum active power variation of the ESS is roughly equal to 799 W, i.e., $\Delta P_{s_{max}} = 799$ W or $P_{s_{max}} = 797$ W. This value is less than its maximum possible active power of approximately 1500 W, therefore the ESS is able to provide active power demand subject to $r_{PV} \in [20, 100]\%$ (or $\underline{H} \in [1, 0.6]$) and caused by load or PV power step disturbances up to $\pm 20\%$ of the load rated active power (± 600 W) relative to the rated operating point.

To summarize, an $\mathcal{H}_\infty$ optimal control solution that is robust in performance under $r_{PV} \in [20, 100]\%$ (or $\underline{H} \in [1, 0.6]$) and with variations of $\pm 15\%$ of the load rated active power (± 450 W) around its steady-state operating point could always be generated.

VIII. CONCLUSION AND PERSPECTIVES

This paper has proposed an $\mathcal{H}_\infty$-based multi-variable robust control design approach for frequency stability in stand-alone MGs with a high RES penetration rate. A hybrid power generation system operating in stand-alone mode has been regarded as a sufficiently representative example of such

MGs, with at least two power sources, either conventional or renewable, and an energy storage unit that must have been coordinated to provide primary frequency ancillary service. The considered problem has been formulated and solved in a systematic manner, yielding the remarkable results listed below

- Topological and nonlinear averaged models of each subsystem have been introduced, followed by linearized frequency-control-oriented modelling of the stand-alone diesel-PV-supercapacitor system. For primary frequency control, a cascaded two-level control structure has been implemented, with classical PI-based current tracking controllers placed on a lower control level and receiving references from an $\mathcal{H}_\infty$-control-based upper level. A comprehensive methodology for casting the specific engineering demands of MG operation into the $\mathcal{H}_\infty$ control formalism has been outlined. Additionally, it has been demonstrated how closed-loop operation requirements must be incorporated into the initial MG configuration and design, specifically in selecting and rating the ESS;
- Numerical simulations performed with MATLAB®/ Simulink® have shown the validity and effectiveness of the proposed frequency robust control strategy on a kVA-rated MG, with the synthesized $\mathcal{H}_\infty$ controller capable of ensuring stable and robust performance caused by load or PV power step disturbances up to $\pm 20\%$ of the load rated active power (± 600 W) with respect to the rated operating point. In addition, the control design parameters can have effectively aided in supercapacitor choice and resizing. Indeed, since the MG frequency variation with the ESS by $\mathcal{H}_\infty$ control has been fixed by the choice of the weighting function $W_{perf_2}(s)$, the imposed dynamic performance requirements can be relaxed in order to increase the MG admissible frequency variation, resulting in power and energy reduction of the storage device, thereby decreasing its investment cost;
- In the presence of multiple PV power step changes and uncertainty levels in the steady-state value of the supercapacitor state of charge SoC_{sc_e} (or supercapacitor voltage V_{sc_e}), a robust performance analysis of the previously designed $\mathcal{H}_\infty$ controller has been conducted. This has pointed out that the synthesized $\mathcal{H}_\infty$ controller remains robust in performance against the entire variation range of $SoC_{sc_e} \in [25, 100]\%$ (or $V_{sc_e} \in [24, 48]$ V) and caused by load or PV power step disturbances up to $\pm 10\%$ of the load rated active power (± 300 W) relative to the rated operating point, which has been quite good for the practical operation of the supercapacitor-based ESS as long as the corresponding variations of the supercapacitor output current and the d-component of the inverter output current are considered admissible;
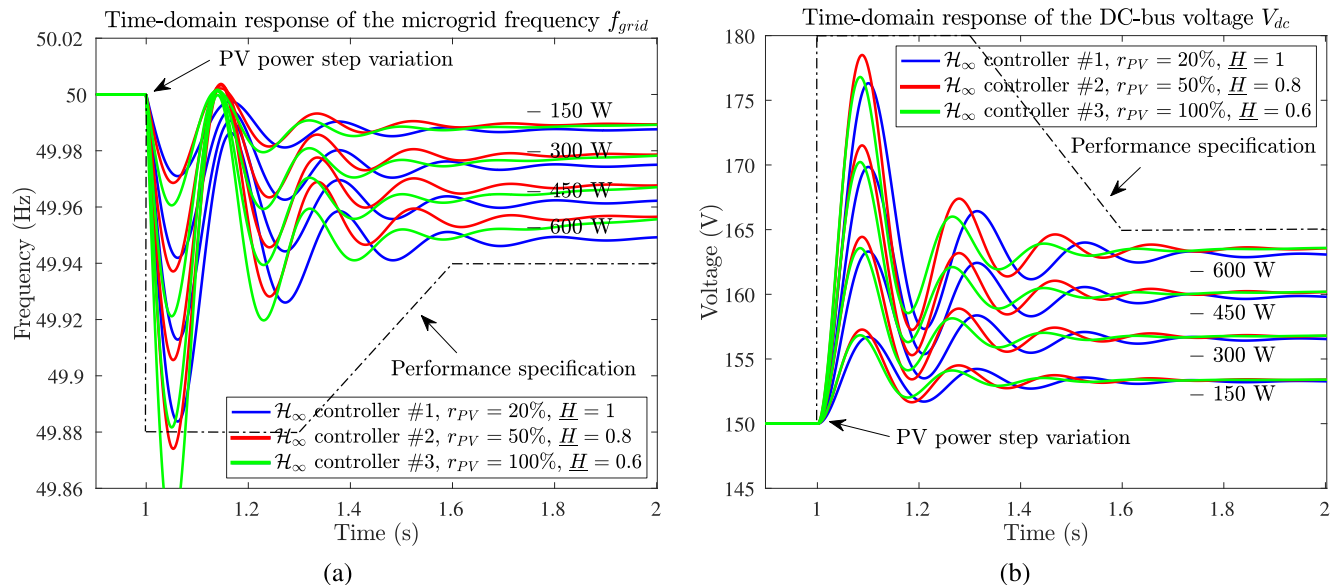
FIGURE 24. (a) MG frequency time-domain response f_{grid} and (b) DC-bus voltage time-domain response V_{dc} under PV power step disturbances ranging from −5% to −20% of the load rated active power (−150 W to −600 W) taking into account the variation in the PV penetration rate r_{PV} (or the MG equivalent inertia constant $\underline{H}$).
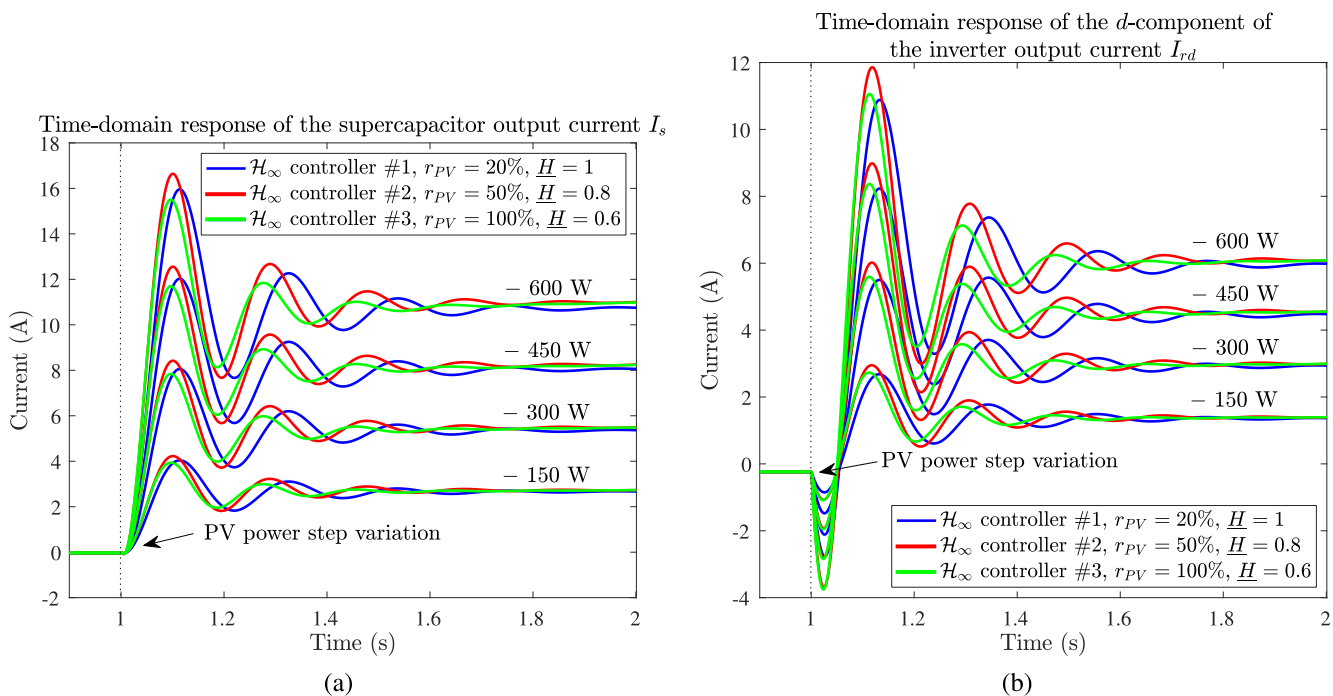

FIGURE 25. Time-domain responses of (a) the supercapacitor output current I_s and (b) the d-component of the inverter output current I_{rd} under PV power step disturbances ranging from −5% to −20% of the load rated active power (−150 W to −600 W) taking into account the variation in the PV penetration rate r_{PV} (or the MG equivalent inertia constant $\underline{H}$).

- Under uncertainty levels in the PV penetration rate $r_{PV} \in [20, 100]\%$ (resulting in considering the MG equivalent inertia constant as a parametric uncertainty $\underline{H} \in [1, 0.6]$) and with load or PV power step changes of ±15% of the load rated active power (±450 W) relative to the rated operating point, an $\mathcal{H}_\infty$ optimal control solution that is robust in performance could have always been designed.

The necessity to know the MG model and the nominal values of MG parameters (e.g., enough mathematical modelling understanding requirement) is a drawback of the proposed control approach; however, the fact that we have afterwards tools to quantify the control robustness can be seen as an advantage in analyzing MG operation scenarios in the presence of parameter uncertainties, interaction dynamics, topology changes, and operating point variations.

TABLE 5. Parameters of the studied MG for frequency control.

Symbol	Description	Value	Unity
	Microgrid		
S_b	Power base unit	2	MVA
H	Simplified equivalent inertia constant	2	MW.s
$\underline{H} = H/S_b$	Per-unitized simplified equivalent inertia constant	1	pu
	Diesel engine generator		
$P_{diesel_{rated}}$	Rated active power	1.6	MW
P_{diesel_e}	Initial active power	1	MW
s_{diesel}	Droop value for primary frequency control	1.5	Hz/MW
$\underline{s_{diesel}} = s_{diesel}\dfrac{S_b}{f_b}$	Per-unitized droop value for primary frequency control	0.06	pu
K_i	Inverse of the response time for secondary frequency control	0.08	MW/Hz
$\underline{K_i} = K_i\dfrac{f_b}{S_b}$	Inverse of the response time in a per-unit frame for secondary frequency control	2	pu
T_{diesel}	Time constant	0.22	s
	Photovoltaic energy source		
$P_{PV_{rated}}$	Rated active power	0.25	MW
P_{PV_e}	Initial active power	0.2	MW
	Aggregated load		
$P_{load_{rated}}$	Rated active power	1.85	MW
P_{load_e}	Initial active power	1.2	MW
D_{load}	Simplified damping constant	0	MW/Hz
$\underline{D_{load}} = D_{load}\dfrac{f_b}{S_b}$	Per-unitized simplified damping constant	0	pu

TABLE 6. Parameters of the test bench for frequency control.

Symbol	Description	Value	Unity
	Microgrid		
S_b	Power base unit	5	kVA
H	Simplified equivalent inertia constant	5	kW.s
$\underline{H} = H/S_b$	Per-unitized simplified equivalent inertia constant	1	pu
	Diesel engine generator		
$P_{diesel_{rated}}$	Rated active power	4	kW
P_{diesel_e}	Initial active power	2.5	kW
s_{diesel}	Droop value for primary frequency control	0.6	Hz/kW
$\underline{s_{diesel}} = s_{diesel}\dfrac{S_b}{f_b}$	Per-unitized droop value for primary frequency control	0.06	pu
K_i	Inverse of the response time for secondary frequency control	0.2	kW/Hz
$\underline{K_i} = K_i\dfrac{f_b}{S_b}$	Inverse of the response time in a per-unit frame for secondary frequency control	2	pu
T_{diesel}	Time constant	0.022	s
	Photovoltaic energy source		
$P_{PV_{rated}}$	Rated active power	0.625	kW
P_{PV_e}	Initial active power	0.5	kW
	Aggregated load		
$P_{load_{rated}}$	Rated active power	4.625	kW
P_{load_e}	Initial active power	3	kW
D_{load}	Simplified damping constant	0	kW/Hz
$\underline{D_{load}} = D_{load}\dfrac{f_b}{S_b}$	Per-unitized simplified damping constant	0	pu

Use of the $\mathcal{H}_\infty$ robust control approach in the presence of large load or PV active power disturbances in the system may not guarantee the imposed dynamic performance specifications. In this situation, the design of an LPV control strategy could be a viable option for addressing diverse operating conditions (e.g., changes in ESS capacity, variability in PV system output power). The advantage of LPV control is that stability and performance of the closed loop can be guaranteed not only for all possible parameter values, but also during variations in the parameters. The LPV controller is capable of automatically adjusting its parameters for various operating points. In addition, the impact of parametric uncertainties, variations in system parameters, device aging, etc., should be analyzed to test the controller robustness.

In the context of energy management, namely load frequency control and power sharing within hybrid MGs composed of hybrid ESSs and inverter-interfaced distributed generators, fuzzy logic frameworks can be frequently integrated with distributed control systems as a leading intelligent tool to choose the proper distributed controller settings [58],

TABLE 7. Parameters of the real supercapacitor-based ESS for frequency control.

| Symbol	Description	Value	Unity
	General characteristics		
$S_{r_{rated}}$	Rated apparent power	≈ 1751	VA
$P_{r_{rated}}$	Rated active power	≈ 1459	W
$U_{r_{rated}}$	Rated output phase-to-phase voltage of the three-phase inverter (chosen)	80	V
$I_{r_{rated}}$	Rated output phase current of the three-phase inverter	≈ 12.6	A
$I_{rd_{max}}$	Maximum value of the d-component of the inverter output current (computed)	≈ 18.2	A
η_{ess}	DC/AC global efficiency of the energy conversion chain	≈ 95	%
	Choke		
L_c	Inductance (catalog)	390	μH
R_c	Resistance (catalog)	11	mΩ
	Chopper		
	IGBTs Semikron SKM200GB123D with $U_{max} = 1200$ V and $I_{max} = 200$ A		
f_{s_c}	PWM switching frequency	≈ 31.4	kHz
	DC bus		
C_{dc}	Capacitance (catalog)	5300	μF
R_{dc}	Resistance (estimated)	1285	Ω
V_{dc}^{ref}	Setpoint value of the voltage (chosen)	150	V
	Three-phase inverter		
	IGBTs Semikron SKM50GAL123D with $U_{max} = 1200$ V and $I_{max} = 50$ A		
f_{s_i}	PWM switching frequency	10	kHz
	Output filter		
L_f	Inductance (catalog)	7	mH
R_f	Resistance (estimated)	440	mΩ
C_f	Capacitance (catalog)	56	μF
	Supercapacitor bank		
	Maxwell BoostCap BMOD0165-P048		
C_{sc}	Capacitance (catalog)	165	F
R_{sc}	Series resistance (estimated)	5.12	mΩ
R_{sc_p}	Parallel resistance (estimated)	1453.9	Ω
$V_{sc_{min}}$	Minimum voltage (chosen)	24	V
$V_{sc_{max}}$	Maximum voltage (chosen)	48	V
$I_{s_{max}}$	Maximum value of the output current (computed)	≈ 64.7	A
$P_{s_{max}}$	Maximum active power (designed)	≈ 1536	W
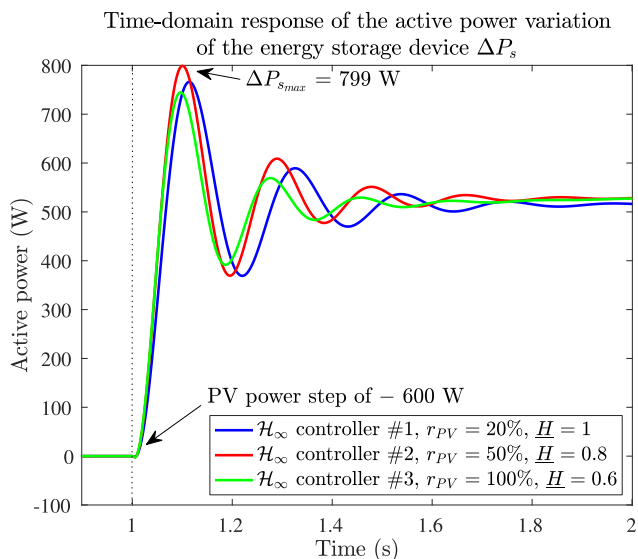
FIGURE 26. Active power variation of the energy storage device ΔP_s under a PV power step disturbance of -20% of the load rated active power (-600 W) taking into account the variation in the PV penetration rate r_{PV} (or the MG equivalent inertia constant $\underline{H}$).

[59], [60], [61]. Such advanced energy management systems can mitigate the frequency excursion due to some parameter uncertainties, short-term grid disturbances, faulted grid conditions, changes in the weather conditions (e.g., PV or wind power fluctuations) or various rates of RESs penetration, operational mode change, communication delays, and achieve desirable power splitting and power sharing accuracy according to different frequency characteristics of a hybrid ESS.

Other possible further directions may concern study of methods to reduce complexity of the resulted controllers, the scalability of the approach and opportunity to apply it in the case of more complex MGs, under various scenarios, including those of considering parameters' variations and/or variable topology.

APPENDIX A
PARAMETERS OF THE STUDIED MICROGRID FOR FREQUENCY CONTROL
See Table 5.

APPENDIX B
PARAMETERS OF THE TEST BENCH FOR FREQUENCY CONTROL
See Tables 6 and 7.

APPENDIX C
PER-UNIT VALUES FOR THE TEST BENCH
See Table 8.

$$\begin{bmatrix} X_d \\ X_q \end{bmatrix} = \sqrt{\frac{2}{3}} \begin{bmatrix} \cos\left(\omega_{grid}t\right) & \cos\left(\omega_{grid}t - \frac{2\pi}{3}\right) & \cos\left(\omega_{grid}t - \frac{4\pi}{3}\right) \\ -\sin\left(\omega_{grid}t\right) & -\sin\left(\omega_{grid}t - \frac{2\pi}{3}\right) & -\sin\left(\omega_{grid}t - \frac{4\pi}{3}\right) \end{bmatrix} \begin{bmatrix} X_1 \\ X_2 \\ X_3 \end{bmatrix}. \tag{13}$$

$$\begin{bmatrix} X_1 \\ X_2 \\ X_3 \end{bmatrix} = \sqrt{\frac{2}{3}} \begin{bmatrix} \cos\left(\omega_{grid}t\right) & -\sin\left(\omega_{grid}t\right) \\ \cos\left(\omega_{grid}t - \frac{2\pi}{3}\right) & -\sin\left(\omega_{grid}t - \frac{2\pi}{3}\right) \\ \cos\left(\omega_{grid}t - \frac{4\pi}{3}\right) & -\sin\left(\omega_{grid}t - \frac{4\pi}{3}\right) \end{bmatrix} \begin{bmatrix} X_d \\ X_q \end{bmatrix}. \tag{14}$$

TABLE 8. Per-unit values for the test bench.

Symbol and expression	Description	Value	Unity
S_b	Power base unit	5	kVA
Base values for AC-side quantities			
$V_b = \sqrt{3}V_r^{ref} = U_r^{ref}$	Voltage base unit	80	V
$I_b = S_b/V_b$	Current base unit	62.5	A
$Z_b = V_b/I_b$	Impedance base unit	1.28	Ω
$f_b = f_{grid}^{ref}$	Frequency base unit	50	Hz
$\omega_b = 2\pi f_b$	Pulsation base unit	100π	rad/s
$L_b = Z_b/\omega_b$	Inductance base unit	4.1	mH
$C_b = 1/(Z_b\omega_b)$	Capacitance base unit	2.5	mF
Base values for DC-side quantities			
$V_{b-dc} = V_b$	Voltage base unit	80	V
$I_{b-dc} = S_b/V_{b-dc} = I_b$	Current base unit	62.5	A
$Z_{b-dc} = V_{b-dc}/I_{b-dc} = Z_b$	Impedance base unit	1.28	Ω
$L_{b-dc} = Z_{b-dc}/\omega_b = L_b$	Inductance base unit	4.1	mH
$C_{b-dc} = 1/(Z_{b-dc}\omega_b) = C_b$	Capacitance base unit	2.5	mF
Per-unit values			
$\underline{V} = V/V_b$	Per-unitized voltage		pu
$\underline{I} = I/I_b$	Per-unitized current		pu
$\underline{Z} = Z/Z_b$	Per-unitized impedance		pu
$\underline{f}_{grid} = f_{grid}/f_b$	Per-unitized frequency		pu
$\underline{\omega}_{grid} = \omega_{grid}/\omega_b$	Per-unitized pulsation		pu
$\underline{L} = L/L_b$	Per-unitized inductance		pu
$\underline{C} = C/C_b$	Per-unitized capacitance		pu
$\underline{P} = P/S_b$	Per-unitized active power		pu
$\underline{Q} = Q/S_b$	Per-unitized reactive power		pu

APPENDIX D
PARK AND INVERSE PARK COORDINATES TRANSFORMATIONS

The Park coordinates transformation used is defined by (13), as shown at the top of the page.

The inverse Park coordinates transformation used is defined by (14), as shown at the top of the page.

REFERENCES

[1] N. Hatziargyriou, H. Asano, R. Iravani, and C. Marnay, "Microgrids," *IEEE Power Energy Mag.*, vol. 5, no. 4, pp. 78–94, Jul./Aug. 2007, doi: 10.1109/MPAE.2007.376583.

[2] D. E. Olivares, A. Mehrizi-Sani, A. H. Etemadi, C. A. Cañizares, R. Iravani, M. Kazerani, A. H. Hajimiragha, O. Gomis-Bellmunt, M. Saeedifard, R. Palma-Behnke, G. A. Jiménez-Estévez, and N. D. Hatziargyriou, "Trends in microgrid control," *IEEE Trans. Smart Grid*, vol. 5, no. 4, pp. 1905–1919, Jul. 2014, doi: 10.1109/TSG.2013.2295514.

[3] T. Goya, E. Omine, Y. Kinjyo, T. Senjyu, A. Yona, N. Urasaki, and T. Funabashi, "Frequency control in isolated island by using parallel operated battery systems applying $\mathcal{H}_\infty$ control theory based on droop characteristics," *IET Renew. Power Gener.*, vol. 5, no. 2, pp. 160–166, Mar. 2011, doi: 10.1049/iet-rpg.2010.0083.

[4] A. M. Howlader, Y. Izumi, A. Uehara, N. Urasaki, T. Senjyu, and A. Y. Saber, "A robust $\mathcal{H}_\infty$ controller based frequency control approach using the wind-battery coordination strategy in a small power system," *Int. J. Electr. Power Energy Syst.*, vol. 58, pp. 190–198, Jun. 2014, doi: 10.1016/j.ijepes.2014.01.024.

[5] Y. W. Li, D. M. Vilathgamuwa, and P. C. Loh, "Robust control scheme for a microgrid with PFC capacitor connected," *IEEE Trans. Ind. Appl.*, vol. 43, no. 5, pp. 1172–1182, Sep./Oct. 2007, doi: 10.1109/TIA.2007.904388.

[6] S. A. Taher and M. Zolfaghari, "Designing robust controller to improve current-sharing for parallel-connected inverter-based DGs considering line impedance impact in microgrid networks," *Int. J. Electr. Power Energy Syst.*, vol. 63, pp. 625–644, Dec. 2014, doi: 10.1016/j.ijepes.2014.06.035.

[7] M. J. Hossain, H. R. Pota, M. A. Mahmud, and M. Aldeen, "Robust control for power sharing in microgrids with low-inertia wind and PV generators," *IEEE Trans. Sustain. Energy*, vol. 6, no. 3, pp. 1067–1077, Jul. 2015, doi: 10.1109/TSTE.2014.2317801.

[8] M. S. Sadabadi, A. Haddadi, H. Karimi, and A. Karimi, "A robust active damping control strategy for an *LCL*-based grid-connected DG unit," *IEEE Trans. Ind. Electron.*, vol. 64, no. 10, pp. 8055–8065, Oct. 2017, doi: 10.1109/TIE.2017.2696501.

[9] T. Kerdphol, F. S. Rahman, Y. Mitani, M. Watanabe, and S. K. Kufeoğlu, "Robust virtual inertia control of an islanded microgrid considering high penetration of renewable energy," *IEEE Access*, vol. 6, pp. 625–636, Nov. 2017, doi: 10.1109/ACCESS.2017.2773486.

[10] T. Kerdphol, F. S. Rahman, M. Watanabe, and Y. Mitani, "Robust virtual inertia control of a low inertia microgrid considering frequency measurement effects," *IEEE Access*, vol. 7, pp. 57550–57560, Apr. 2019, doi: 10.1109/ACCESS.2019.2913042.

[11] M. Armin, M. Rahman, Md. M. Rahman, S. K. Sarker, S. K. Das, Md. R. Islam, A. Z. Kouzani, and M. A. P. Mahmud, "Robust extended $\mathcal{H}_\infty$ control strategy using linear matrix inequality approach for islanded microgrid," *IEEE Access*, vol. 8, pp. 135883–135896, Jul. 2020, doi: 10.1109/ACCESS.2020.3009188.

[12] M. Hamzeh, S. Emamian, H. Karimi, and J. Mahseredjian, "Robust control of an islanded microgrid under unbalanced and nonlinear load conditions," *IEEE J. Emerg. Sel. Topics Power Electron.*, vol. 4, no. 2, pp. 512–520, Jun. 2016, doi: 10.1109/JESTPE.2015.2459074.

[13] D. Zhu and G. Hug-Glanzmann, "Coordination of storage and generation in power system frequency control using an $\mathcal{H}_\infty$ approach," *IET Gener., Transmiss. Distrib.*, vol. 7, no. 11, pp. 1263–1271, Nov. 2013, doi: 10.1049/iet-gtd.2012.0522.

[14] P. Li, X. Yu, J. Zhang, and Z. Yin, "The $\mathcal{H}_\infty$ control method of grid-tied photovoltaic generation," *IEEE Trans. Smart Grid*, vol. 6, no. 4, pp. 1670–1677, Jul. 2015, doi: 10.1109/TSG.2015.2409371.

[15] A. Kahrobaeian and Y. A. R. I. Mohamed, "Suppression of interaction dynamics in DG converter-based microgrids via robust system-oriented control approach," *IEEE Trans. Smart Grid*, vol. 3, no. 4, pp. 1800–1811, Dec. 2012, doi: 10.1109/TSG.2012.2217763.

[16] C. Wang, P. Yang, C. Ye, Y. Wang, and Z. Xu, "Voltage control strategy for three/single phase hybrid multimicrogrid," *IEEE Trans. Energy Convers.*, vol. 31, no. 4, pp. 1498–1509, Dec. 2016, doi: 10.1109/TEC.2016.2595860.

[17] M. Babazadeh and H. Karimi, "A robust two-degree-of-freedom control strategy for an islanded microgrid," *IEEE Trans. Power Del.*, vol. 28, no. 3, pp. 1339–1347, Jul. 2013, doi: 10.1109/TPWRD.2013.2254138.

[18] V. P. Singh, S. R. Mohanty, N. Kishor, and P. K. Ray, "Robust $\mathcal{H}_\infty$ load frequency control in hybrid distributed generation system," *Int. J. Electr. Power Energy Syst.*, vol. 46, pp. 294–305, Mar. 2013, doi: 10.1016/j.ijepes.2012.10.015.

[19] B. E. Sedhom, M. M. El-Saadawi, M. A. Elhosseini, M. A. Saeed, and E. E. Abd-Raboh, "A harmony search-based H-infinity control method for islanded microgrid," *ISA Trans.*, vol. 99, pp. 252–269, Apr. 2020, doi: 10.1016/j.isatra.2019.10.014.

[20] A. Mohanty, M. Viswavandya, S. Mohanty, P. K. Ray, and S. Patra, "Modelling, simulation and optimisation of robust PV based micro grid for mitigation of reactive power and voltage instability," *Int. J. Electr. Power Energy Syst.*, vol. 81, pp. 444–458, Oct. 2016, doi: 10.1016/j.ijepes.2016.02.027.

[21] M. Boukerdja, A. Chouder, L. Hassaine, B. O. Bouamama, W. Issa, and K. Louassaa, "$\mathcal{H}_\infty$ based control of a DC/DC buck converter feeding a constant power load in uncertain DC microgrid system," *ISA Trans.*, vol. 105, pp. 278–295, Oct. 2020, doi: 10.1016/j.isatra.2020.05.031.

[22] Z. Li, C. Zang, P. Zeng, H. Yu, S. Li, and J. Bian, "Control of a grid-forming inverter based on sliding-mode and mixed H_2/H_∞ control," *IEEE Trans. Ind. Electron.*, vol. 64, no. 5, pp. 3862–3872, May 2017, doi: 10.1109/TIE.2016.2636798.

[23] H. R. Baghaee, M. Mirsalim, G. B. Gharehpetian, and H. A. Talebi, "A generalized descriptor-system robust $\mathcal{H}_\infty$ control of autonomous microgrids to improve small and large signal stability considering communication delays and load nonlinearities," *Int. J. Electr. Power Energy Syst.*, vol. 92, pp. 63–82, Nov. 2017, doi: 10.1016/j.ijepes.2017.04.007.

[24] H. R. Baghaee, M. Mirsalim, G. B. Gharehpetian, and H. A. Talebi, "A decentralized robust mixed H_2/H_∞ voltage control scheme to improve small/large-signal stability and FRT capability of islanded multi-DER microgrid considering load disturbances," *IEEE Syst. J.*, vol. 12, no. 3, pp. 2610–2621, Sep. 2018, doi: 10.1109/JSYST.2017.2716351.

[25] S. Gholami, S. Saha, and M. Aldeen, "Robust multiobjective control method for power sharing among distributed energy resources in islanded microgrids with unbalanced and nonlinear loads," *Int. J. Electr. Power Energy Syst.*, vol. 94, pp. 321–338, Jan. 2018, doi: 10.1016/j.ijepes.2017.07.012.

[26] L. Yang and Z. Hu, "Coordination of generators and energy storage to smooth power fluctuations for multi-area microgrid clusters: A robust decentralized approach," *IEEE Access*, vol. 9, pp. 12506–12520, Jan. 2021, doi: 10.1109/ACCESS.2021.3052043.

[27] S. A. Taher, M. Zolfaghari, C. Cho, M. Abedi, and M. Shahidehpour, "A new approach for soft synchronization of microgrid using robust control theory," *IEEE Trans. Power Del.*, vol. 32, no. 3, pp. 1370–1381, Jun. 2017, doi: 10.1109/TPWRD.2016.2596106.

[28] M. Davari and Y. A. R. I. Mohamed, "Robust multi-objective control of VSC-based DC-voltage power port in hybrid AC/DC multi-terminal microgrids," *IEEE Trans. Smart Grid*, vol. 4, no. 3, pp. 1597–1612, Sep. 2013, doi: 10.1109/TSG.2013.2249541.

[29] P. Li, Z. Yin, J. Zhang, and D. Xu, "Modelling robustness for a flexible grid-tied photovoltaic generation system," *IET Renew. Power Gener.*, vol. 9, no. 4, pp. 315–322, May 2015, doi: 10.1049/iet-rpg.2014.0098.

[30] A. Haddadi, B. Boulet, A. Yazdani, and G. Joós, "A μ-based approach to small-signal stability analysis of an interconnected distributed energy resource unit and load," *IEEE Trans. Power Del.*, vol. 30, no. 4, pp. 1715–1726, Aug. 2015, doi: 10.1109/TPWRD.2014.2380788.

[31] Y. Han, P. M. Young, A. Jain, and D. Zimmerle, "Robust control for microgrid frequency deviation reduction with attached storage system," *IEEE Trans. Smart Grid*, vol. 6, no. 2, pp. 557–565, Mar. 2015, doi: 10.1109/TSG.2014.2320984.

[32] H. Bevrani, M. R. Feizi, and S. Ataee, "Robust frequency control in an islanded microgrid: $\mathcal{H}_\infty$ and μ synthesis approaches," *IEEE Trans. Smart Grid*, vol. 7, no. 2, pp. 706–717, Mar. 2016, doi: 10.1109/TSG.2015.2446984.

[33] A. Kahrobaeian and Y. A. R. I. Mohamed, "Direct single-loop μ-synthesis voltage control for suppression of multiple resonances in microgrids with power-factor correction capacitors," *IEEE Trans. Smart Grid*, vol. 4, no. 2, pp. 1151–1161, Jun. 2013, doi: 10.1109/TSG.2012.2228014.

[34] M. Modabbernia, B. Alizadeh, A. Sahab, and M. M. Moghaddam, "Robust control of automatic voltage regulator (AVR) with real structured parametric uncertainties based on $\mathcal{H}_\infty$ and μ-analysis," *ISA Trans.*, vol. 100, pp. 46–62, May 2020, doi: 10.1016/j.isatra.2020.01.010.

[35] A. Kahrobaeian and Y. A. R. I. Mohamed, "Robust single-loop direct current control of LCL-filtered converter-based DG units in grid-connected and autonomous microgrid modes," *IEEE Trans. Power Electron.*, vol. 29, no. 10, pp. 5605–5619, Oct. 2014, doi: 10.1109/TPEL.2013.2294876.

[36] M. S. Sadabadi, Q. Shafiee, and A. Karimi, "Plug-and-play voltage stabilization in inverter-interfaced microgrids via a robust control strategy," *IEEE Trans. Control Syst. Technol.*, vol. 25, no. 3, pp. 781–791, May 2017, doi: 10.1109/TCST.2016.2583378.

[37] M. S. Sadabadi, Q. Shafiee, and A. Karimi, "Plug-and-play robust voltage control of DC microgrids," *IEEE Trans. Smart Grid*, vol. 9, no. 6, pp. 6886–6896, Nov. 2018, doi: 10.1109/TSG.2017.2728319.

[38] Q. L. Lam, A. I. Bratcu, and D. Riu, "Systematic multi-variable $\mathcal{H}_\infty$ control design for primary frequency regulation in stand-alone microgrids with high penetration of renewable energy sources," in *Proc. Eur. Control Conf.*, Jun./Jul. 2016, pp. 1794–1799, doi: 10.1109/ECC.2016.7810551.

[39] Q. L. Lam, A. I. Bratcu, and D. Riu, "Frequency robust control in stand-alone microgrids with PV sources: Design and sensitivity analysis," in *Proc. Symp. Génie Electrique*, Jun. 2016, pp. 1–8. [Online]. Available: https://hal.archives-ouvertes.fr/hal-01361556

[40] Q. L. Lam, "Advanced control of microgrids for frequency and voltage stability: Robust control co-design and real-time validation," Ph.D. dissertation, Université Grenoble Alpes, Grenoble, France, 2018. [Online]. Available: https://tel.archives-ouvertes.fr/tel-01836292

[41] Q. L. Lam, D. Riu, A. I. Bratcu, A. Labonne, and C. Boudinet, "Power hardware-in-the-loop validation of primary frequency robust control in stand-alone microgrids with storage units," *Electr. Eng.*, vol. 105, pp. 317–333, Feb. 2023, doi: 10.1007/s00202-022-01666-6.

[42] G. M. A. Delille, "Contribution du stockage à la gestion avancée des systèmes électriques, approches organisationnelles et technico-économiques dans les réseaux de distribution," Ph.D. dissertation, École Centrale de Lille, Lille, France, 2010. [Online]. Available: https://tel.archives-ouvertes.fr/tel-00586088

[43] A. Kuperman and I. Aharon, "Battery–ultracapacitor hybrids for pulsed current loads: A review," *Renew. Sustain. Energy Rev.*, vol. 15, no. 2, pp. 981–992, Feb. 2011, doi: 10.1016/j.rser.2010.11.010.

[44] P. Thounthong, V. Chunkag, P. Sethakul, S. Sikkabut, S. Pierfederici, and B. Davat, "Energy management of fuel cell/solar cell/supercapacitor hybrid power source," *J. Power Sources*, vol. 196, no. 1, pp. 313–324, Jan. 2011, doi: 10.1016/j.jpowsour.2010.01.051.

[45] Q. L. Lam, A. I. Bratcu, D. Riu, C. Boudinet, A. Labonne, and M. Thomas, "Primary frequency $\mathcal{H}_\infty$ control in stand-alone microgrids with storage units: A robustness analysis confirmed by real-time experiments," *Int. J. Electr. Power Energy Syst.*, vol. 115, Feb. 2020, Art. no. 105507, doi: 10.1016/j.ijepes.2019.105507.

[46] J. Mongkoltanatas, "Participation d'un système de stockage à la stabilité des réseaux insulaires," Ph.D. dissertation, Université de Grenoble, Grenoble, France, 2014. [Online]. Available: https://tel.archives-ouvertes.fr/tel-01316889

[47] M. Sautreuil, "La robustesse: Une nouvelle approche pour l'intégration des systèmes de génération aéronautique," Ph.D. dissertation, Université Joseph Fourier, Grenoble, France, 2009. [Online]. Available: https://tel.archives-ouvertes.fr/tel-00431340

[48] S. Skogestad and I. Postlethwaite, *Multivariable Feedback Control: Analysis and Design*. New York, NY, USA: Wiley, 2005.

[49] G. Delille, B. Francois, and G. Malarange, "Dynamic frequency control support by energy storage to reduce the impact of wind and solar generation on isolated power system's inertia," *IEEE Trans. Sustain. Energy*, vol. 3, no. 4, pp. 931–939, Oct. 2012, doi: 10.1109/TSTE.2012.2205025.

[50] E. M. G. Rodrigues, G. J. Osório, R. Godina, A. W. Bizuayehu, J. M. Lujano-Rojas, and J. P. S. Catalão, "Grid code reinforcements for deeper renewable generation in insular energy systems," *Renew. Sustain. Energy Rev.*, vol. 53, pp. 163–177, Jan. 2016, doi: 10.1016/j.rser.2015.08.047.

[51] X. Luo, J. Wang, J. D. Wojcik, J. Wang, D. Li, M. Draganescu, Y. Li, and S. Miao, "Review of voltage and frequency grid code specifications for electrical energy storage applications," *Energies*, vol. 11, no. 5, p. 1070, Apr. 2018, doi: 10.3390/en11051070.

[52] D. Hernández-Torres, "Commande robuste de générateurs électrochimiques hybrides," Ph.D. dissertation, Université de Grenoble, Grenoble, France, 2011. [Online]. Available: https://tel.archives-ouvertes.fr/tel-00680983

[53] P. Kundur, *Power System Stability and Control*. New York, NY, USA: McGraw-Hill, 1994.

[54] A. Yazdani and R. Iravani, *Voltage-Sourced Converters in Power Systems*. New York, NY, USA: Wiley, 2010.

[55] S. Bacha, I. Munteanu, and A. I. Bratcu, *Power Electronic Converters Modelling and Control*. London, U.K.: Springer-Verlag, 2014.

[56] W. Nwesaty, A. I. Bratcu, and O. Sename, "Power sources coordination through multivariable LPV/$\mathcal{H}_\infty$ control with application to multi-source electric vehicles," *IET Control Theory Appl.*, vol. 10, no. 16, pp. 2049–2059, Oct. 2016, doi: 10.1049/iet-cta.2015.1163.

[57] Q. L. Lam, A. I. Bratcu, D. Riu, and J. Mongkoltanatas, "Multi-variable H-infinity robust control applied to primary frequency regulation in microgrids with large integration of photovoltaic energy source," in *Proc. IEEE Int. Conf. Ind. Technol. (ICIT)*, Mar. 2015, pp. 2921–2928, doi: 10.1109/ICIT.2015.7125529.

[58] F. Ni, L. Yan, J. Liu, M. Shi, J. Zhou, and X. Chen, "Fuzzy logic-based virtual capacitor adaptive control for multiple HESSs in a DC microgrid system," *Int. J. Electr. Power Energy Syst.*, vol. 107, pp. 78–88, May 2019, doi: 10.1016/j.ijepes.2018.11.023.

[59] A. Abazari, M. Babaei, S. M. Muyeen, and I. Kamwa, "Learning adaptive fuzzy droop of PV contribution to frequency excursion of hybrid microgrid during parameters uncertainties," *Int. J. Electr. Power Energy Syst.*, vol. 123, Dec. 2020, Art. no. 106305, doi: 10.1016/j.ijepes.2020.106305.

[60] W. C. de Carvalho, R. P. Bataglioli, R. A. S. Fernandes, and D. V. Coury, "Fuzzy-based approach for power smoothing of a full-converter wind turbine generator using a supercapacitor energy storage," *Electr. Power Syst. Res.*, vol. 184, Jul. 2020, Art. no. 106287, doi: 10.1016/j.epsr.2020.106287.

[61] T. Kerdphol, M. Watanabe, K. Hongesombut, and Y. Mitani, "Self-adaptive virtual inertia control-based fuzzy logic to improve frequency stability of microgrid with high renewable penetration," *IEEE Access*, vol. 7, pp. 76071–76083, Jun. 2019, doi: 10.1109/ACCESS.2019.2920886.

QUANG LINH LAM received the B.Sc. degree in electrical engineering from the University of Danang–University of Science and Technology, Danang, Vietnam, in 2011, the M.Sc. degree in electrical energy from the Grenoble Institute of Technology, Grenoble, France, in 2014, and the Ph.D. degree in electrical engineering from Grenoble Alpes University, Grenoble, in 2017. His current research interests include optimal design and robust control applied to microgrids and energy conversion systems.

DELPHINE RIU received the engineering and Ph.D. degrees in electrical engineering from the Grenoble Institute of Technology, Grenoble, France, in 1999 and 2002, respectively. She is currently a Professor with the Grenoble Institute of Technology. Her current research interests include design and control of embedded electrical systems or microgrids, including production with storage devices.

ANTONETA IULIANA BRATCU (Senior Member, IEEE) received the M.Sc. degree in electrical engineering from Dunărea de Jos University of Galaţi, Galaţi, Romania, in 1996, the Ph.D. degree in control systems and informatics from Université de Franche-Comté de Besançon, Besançon, France, in 2001, and the Habilitation to lead research from Grenoble Alpes University, Grenoble, France, in 2022. She was with the Department of Control Systems and Electrical Engineering, Dunărea de Jos University of Galaţi, from 1996 to 2011. From 2007 to 2009, she was a Postdoctoral Researcher with the Grenoble Electrical Engineering Laboratory, Grenoble. She joined the Grenoble Image Speech Signal and Automatic Control Laboratory, Grenoble, in 2011, where she is currently an Associate Professor. Her current research interests include optimal and robust control applied to energy conversion systems and smart grids.

● ● ●